Journal of Fluids and Structures 25 (2009) 544–566

JOURNAL OF
FLUIDS AND
STRUCTURES

www.elsevier.com/locate/jfs

Interaction between a cantilevered-free flexible plate and ideal flow[☆]

R.M. Howell[a], A.D. Lucey[a,*], P.W. Carpenter[b], M.W. Pitman[a]

[a] *Fluid Dynamics Research Group, Curtin University of Technology, G.P.O. Box U1987, Perth, W.A. 6845, Australia*
[b] *Fluid Dynamics Research Centre, School of Engineering, University of Warwick, Coventry CV4 7AL, UK*

Received 20 December 2007; accepted 17 December 2008

Abstract

We develop a new computational model of the linear fluid–structure interaction of a cantilevered flexible plate with an ideal flow in a channel. The system equation is solved via numerical simulations that capture transients and allow the spatial variation of the flow–structure interaction on the plate to be studied in detail. Alternatively, but neglecting wake effects, we are able to extract directly the system eigenvalues to make global predictions of the system behaviour in the infinite-time limit. We use these complementary approaches to conduct a detailed study of the fluid–structure system. When the channel walls are effectively absent, predictions of the critical velocity show good agreement with those of other published work. We elucidate the single-mode flutter mechanism that dominates the response of short plates and show that the principal region of irreversible energy transfer from fluid to structure occurs over the middle portion of the plate. A different mechanism, modal-coalescence flutter, is shown to cause the destabilisation of long plates with its energy transfer occurring closer to the trailing edge of the plate. This mechanism is shown to allow a continuous change to higher-order modes of instability as the plate length is increased. We then show how the system response is modified by the inclusion of channel walls placed symmetrically above and below the flexible plate, the effect of unsteady vorticity shed at the trailing edge of the plate, and the effect of a rigid surface placed upstream of the flexible plate. Finally, we apply the modelling techniques in a brief study of upper-airway dynamics wherein soft-palate flutter is considered to be the source of snoring noises. In doing so, we show how a time-varying mean flow influences the type of instability observed as flow speed is increased and demonstrate how localised stiffening can be used to control instability of the flexible plate.

Keywords: Fluid-structure interaction; Cantilevered-free flexible plate; Channel flow; Flutter; Unsteady wake; Snoring

1. Introduction

The fluttering of a flag is perhaps the most ubiquitously observed interaction between a solid and fluid and yet this deceptively simple physical system still defies a complete understanding of its dynamics. A formal representation of the

---

[☆] A preliminary version of this paper was presented in the 7th FSI, AE & FIV + N Symposium, within the 2006 ASME PVP Conference in Vancouver, BC, Canada.

[*] Corresponding author.

E-mail address: A.Lucey@Curtin.edu.au (A.D. Lucey).

doi:10.1016/j.jfluidstructs.2008.12.004

canonical fluid–structure system, of which the flag-flutter configuration is one example, is that of a mean flow interacting with a cantilevered flexible surface embedded in the flow and aligned with its direction. This system differs from the flag-flutter example in that the structural forces are dominated by a flexure term whereas for the flag problem this role is played by the tension induced by large-amplitude motions. The phenomena studied herein may be envisaged as vibrations of a fluid-loaded plate for which small-amplitude motions and linear instability are the precursors of sustained flow-induced finite-amplitude oscillations. While this system might seem distant from any useful application, the elucidation of the rich dynamics at work in the model problem is fundamental to our understanding of many real-world problems in fluid–structure interaction. In this paper we develop a new and versatile model of the system and then conduct an investigation of its stability to linear perturbations from an undisturbed mean state. We also apply our findings to a particular biomechanical system that comprises the motion of the soft palate in the human upper airway. Our particular focus is on the characterisation of energy exchanges between flow and solid within the system. We are then able to show how these sum to the overall, or global, amplification or decay of flexible-plate oscillations that is observed as a system response. We remain aware that the present linear study cannot address the well-known sub-critical instability present in such systems. However, the numerical approach that we describe herein can readily be extended to model non-linear motions of the flexible plate.

The pioneering work of Kornecki et al. (1976) on the problem at hand has, over the past decade or so, stimulated the major thrust in research effort that it deserved. Broadly the modelling of such studies divides into one of two types; the flexible plate either resides in an infinite domain of fluid — for examples, see Huang (1995), Yamaguchi et al. (2000a), Watanabe et al. (2002b), Argentina and Mahadevan (2005), Tang and Païdoussis (2006) and Eloy et al. (2007) — or it is embedded in plane-channel flow — for examples, see Aurégan and Depollier (1995), Guo and Païdoussis (2000), Balint and Lucey (2005) and Tetlow and Lucey (2009). Clearly, the unbounded-fluid case can be regarded as the limit of infinite channel height for a centrally located flexible plate. All of these models predict that beyond a threshold, or critical, applied flow speed the flexible plate loses its stability to small-amplitude disturbances through a flutter mechanism. The critical mode for short plates typically comprises a combination of the fundamental and second *in vacuo* eigenmodes of the cantilevered flexible plate. Increasing the plate length reduces the critical speed and raises the order of the *in vacuo* eigenmodes that dominate the composition of the critical mode. For a short plate the flutter mechanism can be attributed to the strong effect of its finiteness that creates a phase shift between the motion of the plate and the forcing fluid pressure. This results in energy transfer between fluid and plate at all flow speeds. Instability sets in when the net transfer is from fluid to plate; this will be demonstrated in the present paper. In contrast, an *infinitely long* flexible plate, subject to potential flow, experiences a pressure signal that is exactly orthogonal to the plate's motion at all pre-instability flow speeds and therefore does not admit irreversible energy transfer; for example, see Carpenter and Garrad (1985), Crighton and Oswell (1991) and the discussion of Lucey and Carpenter (1993a) for the closely related problem of single-sided flow over an *infinitely long* flexible panel. The dynamic instability to which long flexible plates succumb is a Kelvin–Helmholtz type of flutter. At a sufficiently high level of fluid loading two modes coalesce to give a complex-conjugate pair of wave solutions, one of which is highly amplified and the other commensurately damped. At the onset of this type of flutter, it is the modal-coalescence that creates the phase shift between the pressure signal and wall motion which allows the physical transfer of energy from the fluid to the plate. Long cantilevered flexible plates, which are semi-infinite in the limit of streamwise extent, therefore exhibit elements of both types of the aforementioned flutter mechanisms.

The fundamental relationship between local and global instability of fluid–structure systems has been systematically addressed by Doaré and de Langre (2006) building upon Doaré and de Langre (2002) in which the instability of a fluid-conveying pipe was studied. They show when and how local waves, those predicted by a dispersion equation valid for an infinitely long domain, can combine through a process of propagation and reflection in a finite system to yield a global instability. In the present paper, we extract eigenmodes to make predications of global behaviour. However, our numerical simulations effectively model local behaviour and wave reflections through the enforcement of the boundary conditions at each end of the flexible plate. We base the descriptors 'short' and 'long' for the finite system on the value of nondimensional plate length, $\bar{L} = \rho_f L/(\rho h)$, where L is its dimensional length, ρ_f is the fluid density and (ρh) is the mass per unit area of the plate. However, within Doaré and de Langre's framework of 'from waves to modes', the entire range of $\bar{L}$ studied herein would be considered 'short' in that the disturbance wavelengths are of the same order as the length of the flexible plate. Thus, in this paper, the investigation of spatial dependence within a global response can be at sub-wavelength scales.

The present study models ideal flow but can incorporate the effect of channel walls. The explicit omission of viscous effects may seem an extreme assumption. However, the use of unsteady laminar flow in Balint and Lucey (2005) revealed that the flutter instability of a short flexible plate was qualitatively very similar to that predicted using ideal flow. The flow solution used by Balint and Lucey (2005) is restricted to flows at low Reynolds number, whereas an ideal-flow model can be considered as a model for flows at very high, indeed infinite, Reynolds number. Like the majority of previous studies we assume a two-dimensional flow–structure system that has infinite span. The elegant analysis of Eloy et al. (2007) quantified the effect of finite span on plane waves with fronts perpendicular to the flow direction; what results is a correction factor on the pressure field yielded by a two-dimensional analysis. Thus, we can infer that the dynamics predicted by two-dimensional models will have, at the very least, qualitative validity. The system studied herein is closest to the plane-channel configuration investigated in Guo and Païdoussis (2000). We extend their work by modelling the effects of: (a) a central rigid surface at the leading edge of the flexible plate; (b) the singularity present at the leading edge of the flexible plate; (c) spatially varying stiffness in the flexible plate; (d) the wake shed by the motion of the flexible plate; and (e) an unsteady mean flow. We also compare our findings with those from the corresponding unbounded-flow study of Tang and Païdoussis (2006, 2007) who have investigated the foregoing points (b) and (d).

The most significant difference between the present study and those that have preceded it lies in our development and use of a computational model that permits us to conduct numerical simulations of the flow–structure system. This means that we make no presupposition about disturbance form; by contrast, modal studies require that the fluid-loaded deformation of the flexible plate can be constructed accurately from a finite number of pre-selected *in vacuo* plate modes. Our approach also permits us to model transient behaviour that exists prior to a system eigenstate being reached or that results from the use of a time-varying mean flow. We are also able to identify spatially localised dynamics within the system. These are lost in the aggregating process of Galerkin, or modal, methods that only generate global predictions of behaviour and stability.

The geometry modelled is shown in Fig. 1. Ideal flow is assumed and the perturbed flow field modelled using a linearised boundary-element method (BEM) that then yields the perturbation pressure acting on the plate through the linearised unsteady Bernoulli equation. The motion of the flexible plate is modelled using linearised one-dimensional beam theory. The unsteady shed vorticity is modelled using a linearised discrete-vortex method. In the BEM, vortex singularities are used to model the central surface as they capture the discontinuity in tangential velocity across this surface. Although Tang and Païdoussis (2007) recently used a lumped-vortex method, ours is the first time that a continuous vortex distribution has been used for a fully coupled flow–structure interaction for arbitrarily deforming lifting surfaces. The assembled system is then used to conduct a variety of numerical simulations, the results of which map out the response space of the system. However, we also use the computational model to extract directly the eigenmodes of the fluid–structure system using the state-space methods developed by Pitman and Lucey (2009). An equivalent approach was adopted by Argentina and Mahadevan (2005), although they made simplifying assumptions in their flow model in order to develop a tractable system equation. Our computational model allows the full description of fluid loading to be included. Moreover, the accuracy of our system-stability results is ensured because we include all M fluid–structure eigenmodes, where M is the number of collocation points on the plate. Increasing M decreases the error at a monotonically reducing rate as the solution converges to being exact at the limit $M = \infty$.

The paper is laid out as follows. Initially the construction of the numerical model is described and diagnostic variables are introduced. Results from our numerical simulations are then presented that analyse the flutter instabilities observed at low and high mass ratios. Predicted critical-velocity values obtained via our numerical simulations and from other published work are then compared. Further results are then presented that demonstrate the effects on the flutter instability of shed vorticity, a central rigid surface at the leading edge of the flexible plate, channel walls, an unsteady mean flow and distributed stiffness in the flexible plate. The mechanism of all flutter instabilities observed is

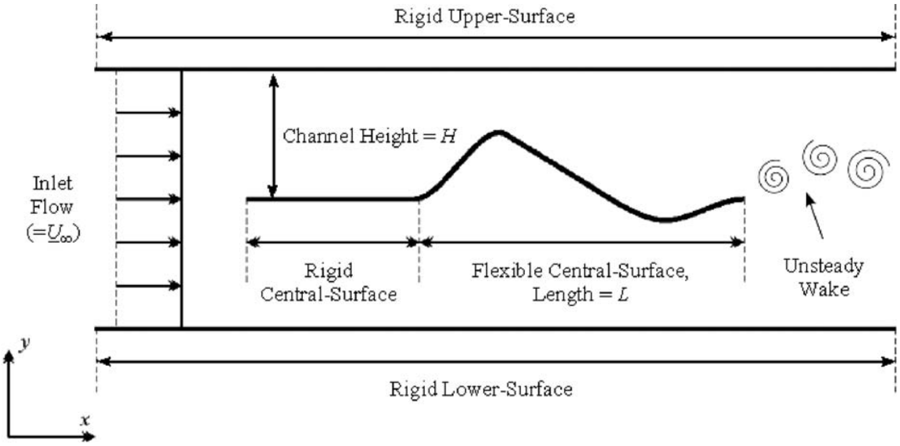

Fig. 1. Schematic of the fluid–structure system studied.

explained in terms of the transfer of fluid energy to the plate via the interaction of the fluid pressure and the plate velocity.

2. Theoretical and computational modelling

The mechanics of the disturbed, linear flow–structure system may be represented by an equation of motion of the form

$$[\mathrm{L}]\eta = -\delta p(\ddot{\eta}, \dot{\eta}, \eta), \tag{1}$$

subject to initial values and plate-edge conditions. [L] is a differential operator on the vertical plate displacement, η; δp is the pressure perturbation due to disturbances to the free-stream flow, U_∞, and is composed of hydrodynamic stiffness, damping and inertia. Co-ordinate axes are as shown in Fig. 1, and Fig. 2 shows how the surfaces of the structure are discretised into a set of boundary-elements or panels, where M_w, M_{cs} and M are the number of panels on the channel walls, rigid central-surface and the flexible plate, respectively. At the centre of each panel is a control point where properties relating to the fluid pressure calculated for each panel are assumed to be located. In contrast, the flexible plate is discretised into a set of $N(= M-1)$ mass points where the mechanical properties of the plate will be assumed centred; these are defined by the panel end points as shown in Fig. 2. Below, we describe the separate plate and flow models and how they are coupled into the final computational model.

2.1. Plate mechanics

The specific spatially discretised form of Eq. (1) for a thin flexible plate is

$$\rho h \ddot{\eta}_n + d\dot{\eta}_n + B\nabla^4 \eta_n = -\delta p_n, \tag{2}$$

where n is the mass-point number along the flexible plate. ρ, h, d and B are, respectively, the density, thickness, damping coefficient and flexural rigidity of the plate. The flexural rigidity is related to the elastic modulus, E, and the Poisson ratio, ν, through

$$B = Eh^3/12(1-\nu^2). \tag{3}$$

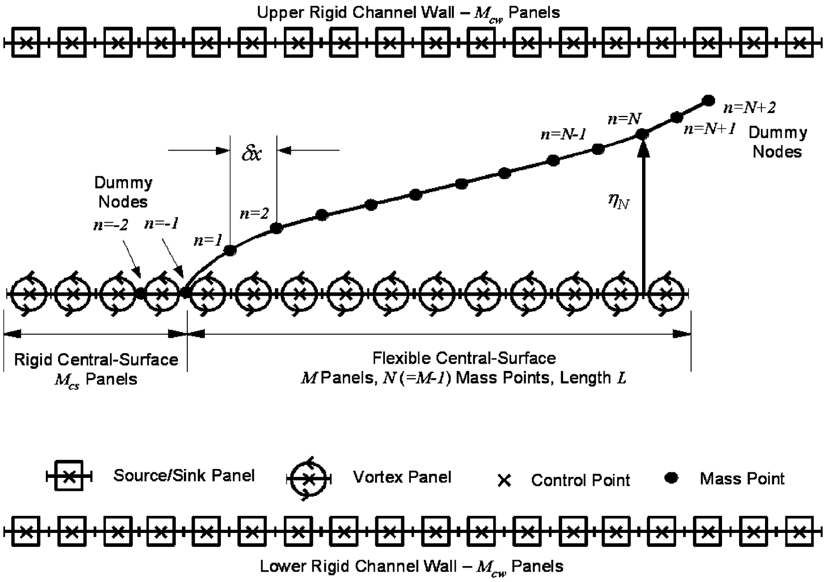

Fig. 2. Fluid–structure system: diagrammatic representation of the computational methods used and the system discretisation.

The flexure term $\nabla^4\eta_n$ is the fourth-order spatial derivative of η_n and can be written in (central) finite-difference form as

$$\nabla^4\eta_n = \frac{6}{\delta x^4}\eta_n - \frac{4}{\delta x^4}(\eta_{n-1} + \eta_{n+1}) + \frac{1}{\delta x^4}(\eta_{n-2} + \eta_{n+2}), \tag{4}$$

where δx is the panel length; for the uniform discretisation used in this paper, $\delta x = L/M$ where L is the length of the flexible plate. Eq. (2) can be rewritten in matrix form as

$$\rho h[\mathbf{I}]\{\ddot{\eta}\} + d[\mathbf{I}]\{\dot{\eta}\} + B[\mathbf{D}_4]\{\eta\} = -\{\delta p\}, \tag{5}$$

where $[\mathbf{I}]$ is the identity matrix and $[\mathbf{D}_4]$ is a pentadiagonal matrix containing the terms generated by Eq. (4). Cantilevered-free edge conditions are enforced on the plate by imposing zero displacement and gradient at the cantilevered end (the leading edge) and zero bending moment and shear force at the free end (the trailing edge); these conditions are implicit in the construction of $[\mathbf{D}_4]$ via their application at the *dummy nodes* labelled $N = -2, -1, N+1$ and $N+2$ illustrated in Fig. 2. Our numerical model of a cantilevered-free plate has been validated by comparing angular frequencies of oscillation of the first six *in vacuo* eigenmodes, as predicted by theory and our computational model; the results of this validation are similar to those presented in Balint and Lucey (2005).

2.2. Fluid mechanics

To calculate the magnitude of the pressure acting on the structural surfaces that is generated by the deflection of the plate, a linearised BEM of flow solution is employed. To apply the BEM, a surface is discretised into a finite number of panels; at the centre of these panels is the panel *control point*. Singularities are distributed along these panels; by determining the strengths of these singularities the pressure at the individual control points can then be calculated. This approach to the fluid-structure interaction of an arbitrarily deforming flexible surface is described in Lucey and Carpenter (1992). The discretisation and singularity distributions utilised in our methodology are illustrated in Fig. 2. We use vortex singularities to model the central surface as they capture the discontinuity in tangential velocity across this lifting surface. In contrast, source/sink singularities are used to model the channel walls as these are non-lifting surfaces. The linearisation of the BEM is also illustrated in this figure: the BEM panels remain fixed on the horizontal, whereas the mass points of the plate are free to travel in the vertical axis. Respectively, the velocity perturbations and perturbation potentials at any control point i on the flexible plate *only* are given by

$$u_i^{T'} = \sum_{m=1}^{M_w} I_{im}^{T\sigma}\sigma_m + \sum_{m=1}^{M_{cs}+M} I_{im}^{T\gamma}\gamma_m + \sum_{m=1}^{M_{cs}+M} I_{im}^{T\lambda}\lambda_m, \tag{6}$$

$$\Phi_i = \sum_{m=1}^{M_w} I_{im}^{\phi\sigma}\sigma_m + \sum_{m=1}^{M_{cs}+M} I_{im}^{\phi\gamma}\gamma_m + \sum_{m=1}^{M_{cs}+M} I_{im}^{\phi\lambda}\lambda_m, \tag{7}$$

where I_{im}^T and I_{im}^ϕ are sets of time-independent influence coefficients that quantify the influence of panel m on panel i; γ_m and λ_m are, respectively, the zero-order and first-order vortex strengths distributed along the central surface and σ_m are the zero-order source/sink strengths distributed along the channel walls. To solve for the singularity strengths, a von Neumann boundary condition is applied so that

$$\left\{\begin{matrix} \Gamma_m \\ \cdots \\ \sigma_m \end{matrix}\right\} = [I_{im}^N]^{-1}\{U_\infty\theta_m + \dot{\eta}_m + u_m^{Nb}\}, \tag{8}$$

where $\Gamma_m = \gamma_m + \lambda_m$. $[I_{im}^N]^{-1}$ contains, in addition to the normal influence coefficients of the singularities, the boundary conditions of: (a) vortex strength continuity at panel end points; and (b) zero vorticity at the plate's trailing edge (thus enforcing the standard Kutta condition for linear displacements of zero pressure difference at the trailing edge). The term θ_m is the panel's angle to the horizontal; as the model is linearised, this can be found through

$$\theta_m = \frac{(\eta_{n+1} - \eta_n)}{\delta x}, \tag{9}$$

where $n = m - 1$. The term $\dot{\eta}_m$ is the panel's vertical speed and u_m^{Nb} is the normal velocity induced by the vortex blobs that model the wake; the latter term is derived below. With the application of the Kutta condition, the effect of the steady vortical wake behind the plate is taken into account. At $t = 0$, the total vorticity in the system, ς, is equal to that bound in the plate and hence

$$\varsigma^{t=0} = \sum_{i=1}^{M_{cs}+M} \gamma_i^{t=0}\delta x_i. \tag{10}$$

In Eq. (10), it is noted that the zero-order, vortex singularity strengths from the panel method, γ_i (first referred to in Eq. (6)) are in units of vorticity per-unit-length; hence the terms γ_i are multiplied by their respective panel lengths δx_i to obtain the addition of each panel to the bound vorticity. Owing to the movement of the flexible plate, the bound vorticity changes with time; the physical effect of this change is to generate an unsteady wake of shed vorticity, its source is the trailing edge of the flexible surface. To model this wake we release a point vortex of strength γ^b (a *vortex blob*) at each time step. Therefore, at any future time t the total vorticity in the system will be equal to the total bound vorticity at that time and any shed vorticity in the wake generated up to that point; hence

$$\varsigma^{t} = \underbrace{\sum_{i=1}^{M_{cs}+M} \gamma_i^{t}\delta x_i}_{\text{bound vorticity at } t} + \underbrace{\sum_{i=1}^{N^b-1} \gamma_i^{b},}_{\text{shed vorticity at } t-1} \tag{11}$$

where N^b is the total number of blobs present in the wake. In Eq. (11), the blob strengths, γ_i^b, are already in units of vorticity because they are the strengths of point vortices. The strength of the blob to be released at time t, $\gamma_{N^b}^b$, is chosen so that the Kelvin condition (that there should be no change in the total vorticity in the system with time) is enforced at each time step. Therefore, $\gamma_{N^b}^b$ is equal to the difference between Eqs. (10) and (11); hence

$$\gamma_{N^b}^b = \sum_{i=1}^{M_{cs}+M} \gamma_i^{t=0}\delta x_i - \left(\sum_{i=1}^{M_{cs}+M} \gamma_i^{t}\delta x_i + \sum_{i=1}^{N^b-1} \gamma_i^{b} \right). \tag{12}$$

It is assumed in this model that the strengths of the blobs do not diminish with time. The effect of the shed blobs on the panels (and each other) is calculated using a discrete-vortex method similar to that detailed in Chorin (1973). In our method the blobs are governed by the two-dimensional Poisson equation such that

$$\nabla^2\psi = -\omega(\underline{x}, t) = -\sum_{n=1}^{N_b} f_{\alpha_n}(\underline{r}_n)\gamma_n^b, \tag{13}$$

where ψ is the stream function, $\omega(\underline{x}, t)$ is the two-dimensional vorticity field, $f_{\alpha_n}(\underline{r}_n)$ is the blob core function and $\underline{r}_n$ is the vector between a blob and the point p that is anywhere in the infinite space away from the blob. A Gaussian approach is used for the core function; this utilises a core size, α_n, for each blob so that the blobs can be coincident without creating a singular result. The Gaussian core function utilised is

$$f_{\alpha_n}(\underline{r}_n) = \frac{1}{\alpha_n^2\pi} \mathrm{e}^{-|\underline{r}_i-\underline{r}_n|^2/\alpha_n^2}, \tag{14}$$

where $\underline{r}_i$ is the distance between a point i on the flexible plate and the point p in space. Utilising Eqs. (13) and (14), the discretised form for the velocity induced at a point i, $\underline{u}_i^b$, owing to the nth blob is

$$\underline{u}_i^b = -\frac{\partial\psi}{\partial r} = u_i^{Tb}\,\underline{i} + u_i^{Nb}\,\underline{j}, \tag{15}$$

where

$$u_i^{Tb} = -\gamma_n^b \frac{y_n}{2\pi|\underline{r}_i - \underline{r}_n|^2}\left(1 - \mathrm{e}^{-|\underline{r}_i-\underline{r}_n|^2/\alpha_n^2}\right), \tag{16}$$

$$u_i^{Nb} = \gamma_n^b \frac{x_n}{2\pi|\underline{r}_i - \underline{r}_n|^2}\left(1 - \mathrm{e}^{-|\underline{r}_i-\underline{r}_n|^2/\alpha_n^2}\right), \tag{17}$$

where x_n and y_n are the horizontal and vertical components of $\underline{r}_n$, respectively; $\underline{i}$ and $\underline{j}$ denote the cartesian components of $\underline{u}_i^b$. A linearised version of the shed vorticity model is deployed in this paper with the blobs assumed only to travel horizontally. Therefore the tangential component of the blob induced velocity, u_i^{Tb}, is zero because y_n is zero; this leads to large computational savings allowing detailed numerical simulations to be executed on a standard desktop computer. In the present application, the magnitude of core size is assumed the same for each blob and is chosen to be $\alpha = 0.4$. Each blob, when created, has its centre placed at a distance of $U_\infty\delta t$ from the trailing edge of the plate where δt is the size of the time step; this is also the assumed distance each blob travels between time steps.

2.3. Fluid–structure coupling

In Lucey et al. (1998) it is shown that when a rotational wake is added to a general flow–structure interaction where the flow is irrotational, the fluid in the region close to the plate remains predominantly irrotational as the rotational fluid is mainly downstream of the trailing edge of the plate. It should be noted, however, that the rotational wake does contribute to the determination of the velocity field adjacent to the moving plate in much the same way that vortex singularities can be used in models of ideal flow with circulation. Therefore, the pressure along the flexible plate can be calculated via the discretised form of the linearised unsteady Bernoulli equation; the pressure difference *across* the plate can be obtained, assuming that the pressure is equal and opposite in value on the upper and lower surfaces of the plate, by multiplying this equation by a factor of two so that we have

$$\delta p_i = -2\rho_f U_\infty u_i^{T'} - \rho_f \frac{\partial \Phi_i}{\partial t}, \tag{18}$$

where ρ_f is the free-stream fluid density. There is no evidence in Eq. (18) that the second part of the pressure has been multiplied by a factor of two; this owes itself to the method employed of calculating Φ_i, given by Eq. (7), that automatically accounts for the pressure difference across the plate with no further alteration. Inserting Eqs. (6)–(8) and (15) into Eq. (18), gives

$$\{\delta p_i\} = -\rho_f \Bigg(\underbrace{2U_\infty'^2[I_{im}^T][I_{im}^N]^{-1}\{\theta_m\} + \dot{U}_\infty'[I_{im}^\phi][I_{im}^N]^{-1}\{\theta_m\}}_{Hydrodynamic\ stiffness} + \underbrace{2U_\infty'[I_{im}^T][I_{im}^N]^{-1}\{\dot{\eta}_m^{av} - u_m^{Nb}\}}_{Hydrodynamic\ damping\ I} + \underbrace{[I_{im}^\phi][I_{im}^N]^{-1}\{U_\infty'\dot{\theta}_m\}}_{Hydrodynamic\ damping\ II} + \underbrace{[I_{im}^\phi][I_{im}^N]^{-1}\{\ddot{\eta}_m - \dot{u}_m^{Nb}\}}_{Hydrodynamic\ inertia} \Bigg), \tag{19}$$

where $U_\infty' = U_\infty + A\sin\omega t$ (allowing the incorporation of an unsteady mean flow) and

$$\dot{\eta}_m^{av} = 0.5(\dot{\eta}_n + \dot{\eta}_{n+1}). \tag{20}$$

The coupled wall-flow system is assembled by introducing the pressure of Eq. (19) into the right-hand side of Eq. (5). Therefore, we have

$$\rho h[\mathbf{I}]\{\ddot{\eta}_m\} + d[\mathbf{I}]\{\dot{\eta}_m\} + B[\mathbf{D_4}]\{\eta_m\} = 2\rho_f U_\infty'^2 \frac{1}{\delta x}[\mathbf{B_1^+}]\{\eta_m\} + \rho_f \dot{U}_\infty' \frac{1}{\delta x}[\mathbf{B_2^+}]\{\eta_m\} + \rho_f U_\infty' \frac{1}{\delta x}[\mathbf{B_2^+}]\{\dot{\eta}_m\} + \rho_f U_\infty'[\mathbf{B_1^-}]\{\dot{\eta}_m\} + \rho_f[\mathbf{B_2}]\{\ddot{\eta}_m\} - 2\rho_f U_\infty'[\mathbf{B_1}]\{u_m^{Nb}\} - \rho_f[\mathbf{B_2}]\{\dot{u}_m^{Nb}\}, \tag{21}$$

where the **[B]** matrices are suitably rearranged forms of the influence matrices presented in Eq. (19) to allow, via the use of the relations in Eqs. (9) and (20), the expression of the fluid–structure system solely in terms of plate acceleration, velocity and displacement, and blob induced acceleration and velocity. The hydrodynamic pressures computed using Eq. (19) are evaluations at the control points of the plate panels, whereas the pressures in Eq. (5) are calculated at the mass points; this introduces a small numerical error that reduces as the discretisation of the plate is increased. Eq. (21) can be re-arranged to give the system equation

$$\{\ddot{\eta}_m\} = [\mathbf{E}]\{\dot{\eta}_m\} + [\mathbf{F}]\{\eta_m\} - [\mathbf{G}]\{u_m^{Nb}\} - [\mathbf{H}]\{\dot{u}_m^{Nb}\}, \tag{22}$$

where

$$[\mathbf{E}] = [\rho h[\mathbf{I}] - \rho_f[\mathbf{B_2}]]^{-1}\left[2\rho_f U_\infty'[\mathbf{B_1^-}] + \rho_f U_\infty' \frac{1}{\delta x}[\mathbf{B_2^+}] - d[\mathbf{I}]\right], \tag{23}$$

$$[\mathbf{F}] = [\rho h[\mathbf{I}] - \rho_f[\mathbf{B_2}]]^{-1}\left[2\rho_f U_\infty'^2 \frac{1}{\delta x}[\mathbf{B_1^+}] + \rho_f \dot{U}_\infty' \frac{1}{\delta x}[\mathbf{B_2^+}] - B[\mathbf{D_4}]\right], \tag{24}$$

$$[\mathbf{G}] = [\rho h[\mathbf{I}] - \rho_f[\mathbf{B_2}]]^{-1}[2\rho_f U_\infty'[\mathbf{B_1}]], \tag{25}$$

$$[\mathbf{H}] = [\rho h[\mathbf{I}] - \rho_f[\mathbf{B_2}]]^{-1}[\rho_f[\mathbf{B_2}]]. \tag{26}$$

2.4. Solution methods

Two distinct, but complementary, approaches are used to solve the system equation. In the first, a time-stepping numerical integration is performed to yield numerical simulations of the system response to an initial form of imposed excitation. Such simulations are able to capture transient effects and permit localised dynamics to be investigated through the analysis of a series of numerical experiments. However, this approach is not so well suited to the prediction of long-time system response and its global mapping. Thus, for the second approach we assume a single-frequency system response that might be expected in the infinite-time limit after all transient oscillations of the plate have decayed. We are then able to use a state-space method that permits the direct extraction of the fluid–structure eigenmodes from the system equation.

The numerical simulations presented in this paper are produced using a semi-implicit method of solution of Eq. (22); this applies Gauss–Siedel sweeps over the internal mass points, utilising the following simplified predictor–corrector relations:

$$\{\dot{\eta}_i^{t+\delta t}\} \approx \{\dot{\eta}_i^t\} + \delta t \frac{\{\ddot{\eta}_i^t + \ddot{\eta}_i^{t+\delta t}\}}{2}, \quad \{\eta_i^{t+\delta t}\} \approx \{\eta_i^t\} + \delta t \frac{\{\dot{\eta}_i^t + \dot{\eta}_i^{t+\delta t}\}}{2} \tag{27,28}$$

to yield converged values of acceleration, velocity and displacement for every mass point at each time step in the evolution of the disturbed system.

Global predictions of the infinite-time system behaviour are generated using a standard state-space method, implemented in a similar way to that detailed by Pitman and Lucey (2009). As applied in this paper, we do not incorporate the effects of the downstream wake nor of an unsteady free-stream. The matrices in Eq. (22) are re-arranged as a *companion-form* matrix from which the eigenvalues and vectors of the coupled system can be extracted directly and the values of critical velocity can be identified. Thus re-writing Eq. (22), having neglected the wake terms, we have

$$\left\{\frac{d^2\eta_m}{dt^2}\right\} - [\mathbf{E}]\left\{\frac{d\eta_m}{dt}\right\} - [\mathbf{F}]\{\eta_m\} = 0. \tag{29}$$

The following substitutions are made

$$w_1(t) = \eta(t) \quad \text{and} \quad w_2(t) = \frac{d\eta}{dt} = \dot{w}_1(t). \tag{30a,b}$$

Inserting relations Eqs. (30a) and (30b) into Eq. (29) yields

$$\{\dot{w}_2\} - [\mathbf{E}]\{w_2\} - [\mathbf{F}]\{w_1\} = 0. \tag{31}$$

Rearranging Eq. (31) for $\dot{w}_2$ we have

$$\{\dot{w}_2\} = [\mathbf{F}]\{w_1\} + [\mathbf{E}]\{w_2\}. \tag{32}$$

Eqs. (30) and (32) lead to a system state equation

$$\begin{Bmatrix} \dot{w}_1 \\ \dot{w}_2 \end{Bmatrix} = \begin{bmatrix} 0 & I \\ F & E \end{bmatrix} \begin{Bmatrix} w_1 \\ w_2 \end{Bmatrix}, \tag{33}$$

that is more simply expressed as

$$\dot{w} = [H]w, \tag{34}$$

where $[H]$ is the companion matrix. Single-frequency response is then assumed and thus

$$\{w\} = \{W\}\exp(\omega t), \tag{35}$$

where ω is a complex eigenvalue of $[H]$ and $\{W\}$ is the eigenvector corresponding to ω that is used to generate the displacement of the plate. Thus,

$$\omega = \omega_R + \mathrm{i}\omega_I \quad \text{and} \quad W = W_R(x) + \mathrm{i}W_I(x). \tag{36a,b}$$

To calculate the plate displacement $\{\eta\}$, only the real part of the first N terms of $\{w\}$ are required; this is found by substituting Eqs. (36a) and (36b) into Eq. (35) giving

$$\eta = \Re(w) = \exp(\omega_R t)(W_R(x)\cos(\omega_I t) - W_I(x)\sin(\omega_I t)). \tag{37}$$

2.5. Diagnostics

To assist in the interpretation of the results presented in this paper, definitions of diagnostic variables are now made. The physical significance of these variables is detailed in the results section when they are used to investigate the fluid–structure phenomena encountered. It is shown in Balint and Lucey (2005) that multiplying Eq. (5) by $\dot{\eta}$ and then integrating over the length of the flexible plate yields the following energy-evolution equation for the fluid-loaded plate

$$\frac{\mathrm{d}}{\mathrm{dt}}\left(\underbrace{\frac{1}{2}\rho h\int_0^L \dot{\eta}^2\mathrm{d}x}_{E_k}+\underbrace{\frac{1}{2}B\int_0^L \eta_{,xx}^2\mathrm{d}x}_{E_s}\right)=\underbrace{\int_0^L(-\delta p)\dot{\eta}\mathrm{d}x}_{\dot{W}}-\underbrace{d\int_0^L \dot{\eta}^2\mathrm{d}x}_{\dot{D}}, \tag{38}$$

where E_s and E_k are the strain and kinetic energies of the flexible plate, respectively, and the total energy, E_t, is equal to E_s+E_k; $\dot{W}$ and $\dot{D}$ are, respectively, the rate of work done by the fluid in the flexible plate and the energy-dissipation rate by structural damping within the plate. The total work done over a particular time period t_p is $W(t_p)=\int_0^{t_p}\dot{W}(t)\,dt$. Both $E_t(t_p)$ and $W(t_p)$ are plotted in nondimensional form

$$\bar{E}_t(t_p)=\frac{E_t(t_p)}{E_s(0)}\quad\text{and}\quad\bar{W}(t_p)=\frac{W(t_p)}{E_s(0)}. \tag{39a,b}$$

Time, free-stream velocity and plate damping are nondimensionalised using the method described in Crighton and Oswell (1991) for an isolated, infinitely long flexible surface, so that

$$\bar{t}=t\frac{\rho_f^2B^{1/2}}{(\rho h)^{5/2}},\quad \bar{U}=U_\infty\frac{(\rho h)^{3/2}}{\rho_f B^{1/2}}\quad\text{and}\quad\bar{d}=d\frac{(\rho h)^{3/2}}{\rho_f^2B^{1/2}}. \tag{40a,b,c}$$

In the present study the flexible surface is not infinitely long, nor is it isolated and thus two further nondimensional parameters are required; these are the nondimensional length (or mass ratio), $\bar{L}$, and the nondimensional channel height, $\bar{H}$, defined by

$$\bar{L}=\frac{\rho_f L}{\rho h}\quad\text{and}\quad\bar{H}=\frac{H}{L}, \tag{41a,b}$$

where H is the distance from the central surface to either channel wall as shown in Fig. 1. Thus in the absence of structural damping the three control parameters for the fluid–structure system are $\bar{U}$, $\bar{L}$ and $\bar{H}$. When plotting data we use the following nondimensional forms

$$\bar{\eta}=\frac{\eta}{\eta_0},\quad \bar{x}=\frac{x}{L},\quad \bar{\delta p}=\frac{\delta p}{\rho_f U_\infty^2},\quad \bar{\dot{\eta}}=\frac{\dot{\eta}}{U_\infty},\quad \bar{\omega}=\omega\frac{(\rho h)^{5/2}}{\rho_f^2B^{1/2}}, \tag{42a,b,c,d,e}$$

where η_0 is the maximum value of η when the plate is initially deflected to provide excitation to the fluid–structure system. Here, ω is the angular frequency of oscillation of the flexible surface and it is nondimensionalised using the scheme adopted for time in Eq. (40a); however, a second scheme of nondimensionalisation of ω, $\bar{\bar{\omega}}$, is used in the following discussion, where ω is divided by the angular frequency of oscillation of the second *in vacuo* eigenmode, ω_2:

$$\bar{\bar{\omega}}=\frac{\omega}{\omega_2}. \tag{43}$$

This permits an easier physical grasp of the effect of the fluid loading on the oscillations of the flexible plate.

3. Results

We first present results for the much-studied case of an isolated flexible plate. This requires moving the upper and lower walls apart until they no longer influence the system dynamics; a value of $\bar{H}=1$ is shown to achieve this, see Howell et al. (2004). This leaves just two control parameters, $\bar{U}$ and $\bar{L}$, that determine the system response. Our goal is to find the critical flow speed, $\bar{U}_c$, beyond which flutter first sets in and identify the mechanism that causes the unstable behaviour. We then explore variations to critical speed and instability mechanism from this ‘standard case’ that occur through the introduction of: (a) an unsteady wake, (b) a rigid-inlet surface, (c) channels walls, (d) temporal variation of the mean flow, and (e) variable plate stiffness. The last two variations are presented with reference to human snoring.

Although all results are presented within the nondimensional framework of Section 2.5, illustrative physical properties used in Sections 3.1 and 3.2 are $L = 1.355\,\mathrm{m}$, $\rho = 2710\,\mathrm{kg/m^3}$, $h = 0.5\,\mathrm{mm}$, $E = 7 \times 10^7\,\mathrm{N/m^2}$, $d = 9.08 \times 10^{-2}\,\mathrm{N\,s/m^3}$; therefore, to give $\bar{L} = 1$ a value of $\rho_f = 1\,\mathrm{kg/m^3}$ is required. Variations to $\bar{L}$ were effected by varying ρ_f; this permits a fixed discretisation, $M = 50$, of the flexible plate to be used that maintains constant numerical accuracy. The numerical simulations require an initial excitation to the fluid–structure system. This is provided by releasing the flexible plate from an imposed deflection at $t = 0$. The deflection form used is that of the second *in vacuo* eigenmode of the cantilevered-free plate. Of course, any other initial form could have been used to the same effect after the passage of sufficient time. We have chosen this mode because, it will be shown, it bears a close resemblance to the critical mode for low $\bar{L}$ and thereby reduces the time taken for the system to arrive at its quasi-steady state.

3.1. *Isolated flexible plate:* $0.2 \leqslant \bar{L} \leqslant 1000$, $\bar{H} = 1$

We first consider the case of $\bar{L} = 1$. Fig. 3(a) shows the system eigenvalues obtained using our state-space method. We have plotted just the two eigenvalues with the lowest frequencies although all $M = 50$ eigenmodes of the system are present in the calculation. Thus, there is no *a priori* selection of modes that contribute most strongly to the system solution. The morphology of the state-space is similar to that obtained by Guo and Païdoussis (2000) and Eloy et al. (2007). We note the second mode (marked 2) of the fluid–structure system is the first to become unstable, $\bar{\omega}_R > 0$ for $\bar{U} > \bar{U}_c = 5.452$, with a non-zero oscillation frequency, $\bar{\omega}_I$, that indicates flutter. Thus, the magnitude of the restorative structural force of the plate exceeds that of pressure loading throughout the flow-speed range. In contrast, for the first mode (marked 1) there is a range of flow speeds for which the flexible plate adopts a mode shape (not presented in this paper) in which its restorative forces almost exactly balance the pressure loading and non-oscillatory damped behaviour occurs. For flexible plates held at both ends, this type of force balance leads to the onset of divergence instability. In the present cantilevered-free configuration its negative $\bar{\omega}_R$ throughout the flow-speed range means that Mode 1 would not feature in the long-term response of the physical system. Fig. 3(b) shows the corresponding system eigenvalues when some damping, $\bar{d} = 5$, is present. Contrasting this with the elastic plate result of Fig. 3(a), it is seen that while second-mode flutter continues to be the critical instability, its onset flow speed has been significantly increased. The fact than energy dissipation through damping can be used to control the instability strongly suggests that the flutter mechanism owes itself to the rate of irreversible energy transfer from flow to structure. This will be confirmed in the investigation that follows immediately below.

We now focus on the form and cause of the flutter instability seen in Fig. 3 for $\bar{L} = 1$. Figures 4(a)–(c) show results obtained at the critical speed for which $\bar{U} = 5.452$. The oscillation of the plate is depicted in Fig. 4(a) as a sequence of snapshots of the flexible plate. An oscillatory, neutrally stable, steady state evolves from the markedly different shape of the initial excitation. It can be shown, using a Fourier analysis, that this critical mode can be made up of 33% and 63% of the first two *in vacuo* eigenmodes based upon strain-energy content, the remainder coming from higher-order modes. The dominant contribution of the first two *in vacuo* modes in combination accounts for the necking seen in the envelope of oscillation. The value of $\bar{\bar{\omega}}$ for this critical mode is 0.69; the effect of the fluid is therefore to reduce the plate's angular frequency of oscillation from that of the second *in vacuo* mode by 31%. Figure 4(b) shows that after an initial drop in

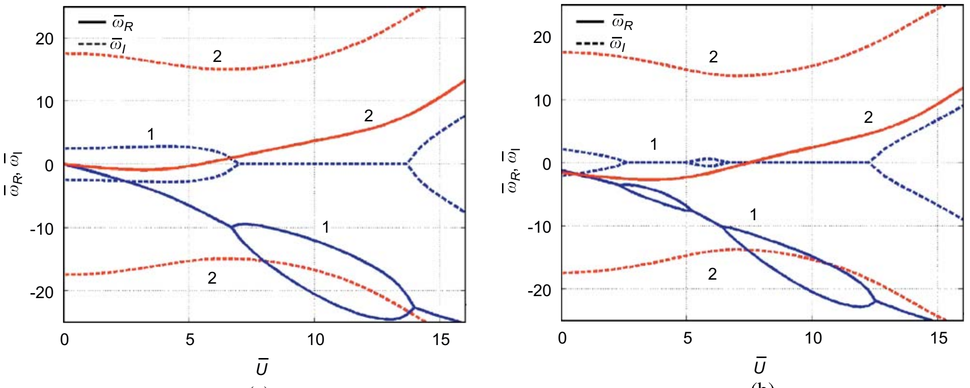

(a) (b)

Fig. 3. Fluid–structure behaviour at $\bar{L} = 1$, $\bar{H} = 1$ (effectively isolated): variation of system eigenmodes with flow speed where (a) elastic plate, $\bar{d} = 0$, and (b) including structural damping with $\bar{d} = 5$. The numbers in each figure identify the mode number in order of ascending frequency at $\bar{U} = 0$.

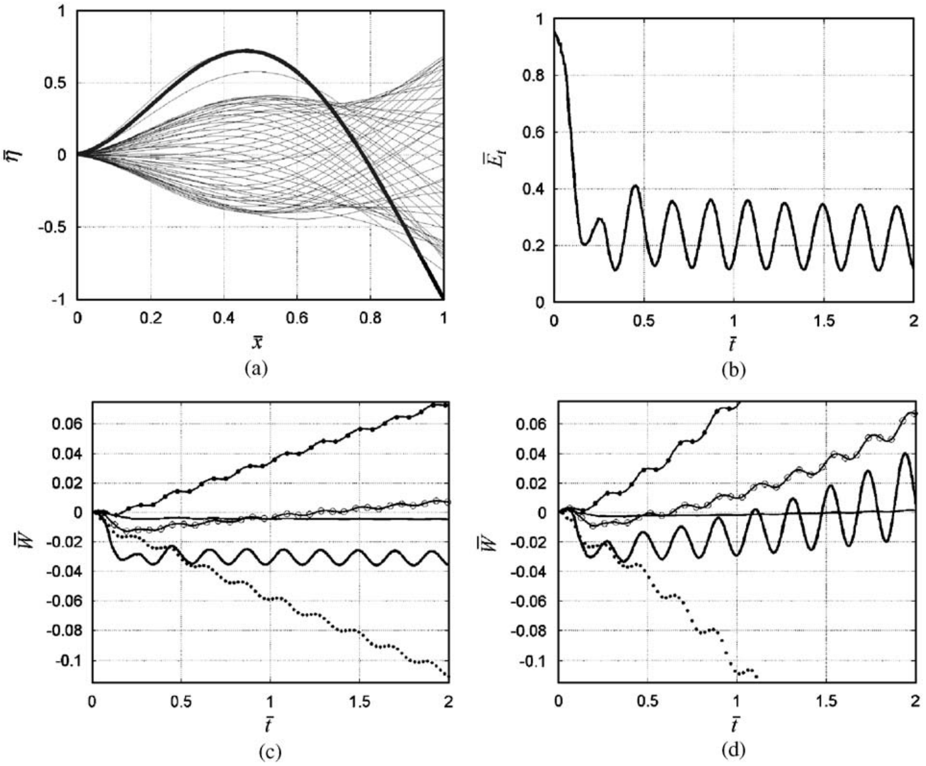

Fig. 4. Fluid–structure behaviour at $\bar{L} = 1$, $\bar{H} = 1$ (effectively isolated): numerical simulations of system behaviour with $\bar{d} = 0$ at the critical flow speed $\bar{U}_c = 5.452$, (a) time-sequence of instantaneous plate deformation (the thick line is the initially imposed deformation), (b) time-variation of plate energy, $\bar{E}_t$, (c) time-variation of work done by fluid on plate, $\bar{W}$, and, for a post-critical flow speed $\bar{U} = 6.0$, (d) time-variation of work done by fluid on plate, $\bar{W}$. In both (c) and (d) the lines —— (thin), -○-, -●- and ···, respectively, indicate the work done over the first, second, third and fourth quarters of the plate from its leading edge, while —— (thick) is the sum of these contributions.

the plate's total energy, $\bar{E}_t$, associated with its evolution from the applied initial condition to system eigenstate, a steady state is achieved. This confirms the neutral stability of the plate's oscillation at this critical speed.

We now consider the energy transfers that underpin this time-series of the plate's energy. Figures 4(c) and (d), respectively, show the time-variation of the work done by the fluid-flow on the plate for two cases: exactly at the critical speed ($\bar{U}_c = 5.452$) and at just above the critical speed ($\bar{U} = 6.0$). In each case, the total work done on the entire length of the flexible plate is plotted and the work done in each of the four quarters $\bar{x} : 0 \to 0.25$, $\bar{x} : 0.25 \to 0.5$, $\bar{x} : 0.5 \to 0.75$ and $\bar{x} : 0.75 \to 1$, of the plate that when summed yield the total. This breakdown, into just four quarters, gives a broad indication of how energy transfer varies along the plate. At the critical speed it is seen that the work done is negative at early times; the energy transfer is from plate to fluid as the deformation evolves from that of the initial condition. Thereafter the change to the mean value of total work done is zero; this again confirms the neutral stability of the system at $\bar{U} = \bar{U}_c = 5.452$. However, we also note that, in the steady state, energy transfer *to* the middle part of the plate (second and third quarters) continuously occurs while for the downstream (fourth) quarter there is energy transfer *from* the plate to the fluid that exactly counterbalances the former. It is the combination of these local effects that yields the global neutral stability of the mode. Just above the critical flow speed, Fig. 4(d) shows that the mean value of total work done by the fluid on the plate increases exponentially. The resulting energy transfer is the cause of the instability. However, we again note that it is the fluid–structure interaction in the middle half of the flexible plate that accounts for the overall unstable behaviour. The downstream quarter of the plate is actually doing work on the fluid. The location of destabilising energy transfer leads us to describe the instability under inspection here ($\bar{L} = 1$ and $\bar{H} = 1$) as being *mid-plate-driven*.

The energy transfers described immediately above arise from the term $\dot{W}$ in the energy equation, Eq. (38). For energy transfer to occur, the product of the terms in the integrand must yield a non-zero result when integrated over a period of oscillation. The time-variations of the terms $(-\delta p)$ and $\dot{\eta}$, in nondimensional form, are plotted in Fig. 5 for three locations on the flexible plate during the numerical simulation of the critical mode that produced Figs. 4(a)–(c). At early

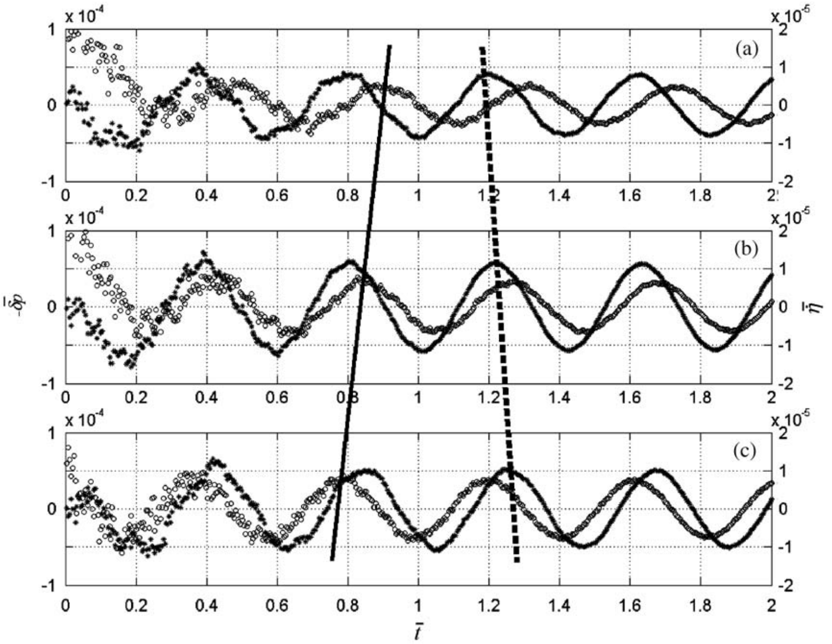

Fig. 5. Fluid–structure behaviour at $\bar{L} = 1$, $\bar{H} = 1$ (effectively isolated): variation of perturbation pressure, $-\delta\bar{p}$ (denoted ○), and plate velocity, $\dot{\bar{\eta}}$ (denoted ✱) with time at (a) $\bar{x} = 0.3$, (b) $\bar{x} = 0.5$, and $\bar{x} = 0.7$ for the numerical simulation that yielded Figs. 4(a)–(c) at the critical flow speed. The added lines —— and – – –, respectively, connect peaks of $-\delta\bar{p}$ and $\dot{\bar{\eta}}$ to illustrate the spatial variation of the phase between these terms.

times modal evolution is again seen. For times in the ensuing steady state, the broken lines that we have sketched in connect corresponding peaks in each of the pressure and plate velocity signals for the three locations. These lines serve to illustrate the spatial variation of the phase relationship between these terms. If the pressure and velocity signals were exactly orthogonal, then there will be no work done over one cycle of oscillation; it is the phase variations to this situation that create the irreversible energy transfers captured in Fig. 4(c) and which underpin the flutter instability represented by Fig. 4(d). The foregoing phase-shifts, away from the orthogonality that would be expected for an infinitely long flexible surface in potential flow, are caused by plate finiteness that combines two effects: those of the leading-edge singularity and the trailing-edge Kutta condition. The relationship between the pressure and velocity at a point on the plate is then uniquely defined by its spatial relationship to the source of these two effects. For one-sided fluid flow over a finite flexible surface, this feature is explained in Lucey and Carpenter (1993a). It will be seen in Section 3.2 that distancing the leading-edge singularity from the flexible plate through the introduction of an upstream rigid surface causes a significant modification to the plate's response and thus destabilisation occurs through an instability mechanism characteristic of a long plate. The mechanism at work for Fig. 4 is essentially the same as that found by Balint and Lucey (2005) for the case of viscous flow destabilising a cantilevered flexible plate through flutter. Finally we remark that the inclusion of material damping leads to a non-zero value of the term $\dot{D}$in Eq. (38). This subtracts from the rate of energy transfer from fluid flow to the flexible plate and therefore increases the value of the critical speed, as seen in Fig. 3(b).

Results that demonstrate the effect of the mass ratio, $\bar{L}$, are now presented. Figure 6 shows the variation of system eigenmodes with flow speed for the present case over four decades of $\bar{L}$ (noting that Fig. 6(a) is a reproduction of Fig. 3(a)). Far lower dimensional and nondimensional critical speeds and oscillation frequencies ensue as $\bar{L}$ is increased; this can be seen in the axis labelling in the progression from Figs. 6(a)–(d). In dimensional terms, large $\bar{L}$ can represent either a significantly increased fluid loading (for a fixed plate length) or an increased plate length (for a fixed fluid density). Each of these increases the ratio of fluid pressure forces to the opposing restorative forces in the flexible plate (as compared with the dynamics of a short plate near its critical speed). Accordingly, the type of instability that yields the critical speed changes from the single-mode flutter in Fig. 6(a) to a modal-coalescence flutter associated with heavy fluid loading. Thus, in Fig. 6(b) it is clearly the coalescence of the second and third modes that leads to the ω_R-branch of the second mode turning to enter the positive quadrant. Correspondingly, the ω_R-branch of the third mode dips downwards to give an increasingly damped solution. For elastic plates held at both ends, exact coalescence of the

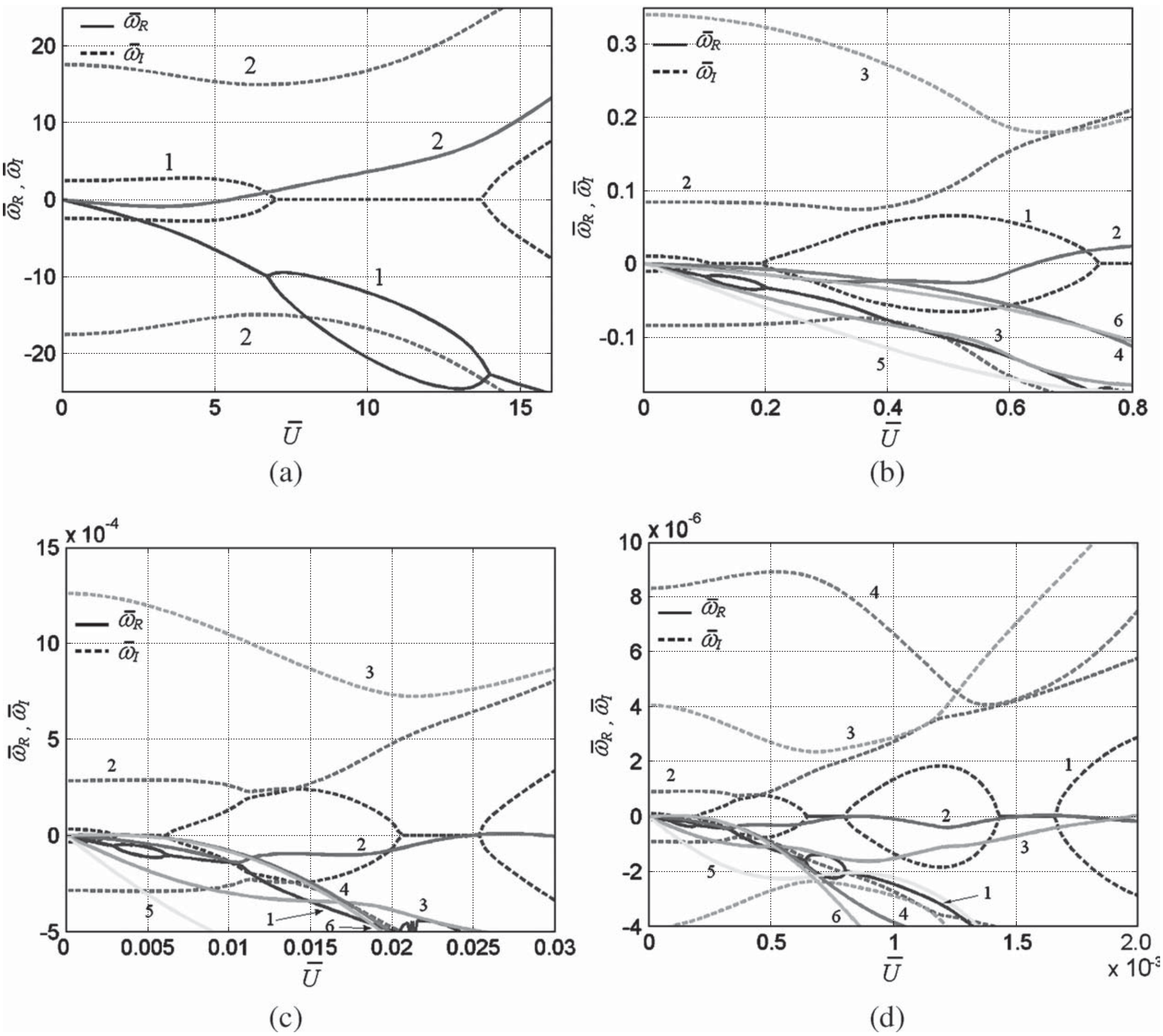

Fig. 6. Fluid–structure behaviour for various $\bar{L}$ at $\bar{H} = 1$ (effectively isolated): variation of system eigenmodes with flow speed for $\bar{d} = 0$ for (a) $\bar{L} = 1$ (as in Fig. 3(a)), (b) $\bar{L} = 10$, (c) $\bar{L} = 100$, and (d) $\bar{L} = 1000$. The numbers in each figure identify the mode number in order of ascending frequency at $\bar{U} = 0$.

interacting modes occurs to give a complex-conjugate pair of solutions; for example, see Weaver and Unny (1970) and Lucey and Carpenter (1993b). Pitman and Lucey (2009) showed that the introduction of structural damping prevents exact coalescence in the panel-flutter problem but the system continues to yield what remains essentially a single-frequency response comprising a highly amplifying and a highly attenuated pair of roots. Of course, only the amplifying root would have significance in a physical system. Exact coalescence can occur only in a wholly conservative system. The present system has been shown to support nonconservative energy transfers and these act in much the same way as does the introduction of damping in the panel-flutter problem. Nevertheless the instability mechanism remains fundamentally of the modal-coalescence type. With a further increase to $\bar{L} = 100$ in Fig. 6(c), it is again the coalescence of second and third modes that results in instability. At $\bar{L} = 1000$ in Fig. 6(d), the coalescence is seen to be more complex involving all of the second, third and fourth modes. The progression to higher-order *in vacuo* eigenmodes participating in the composition of the critical mode as $\bar{L}$ is increased is clearly demonstrated in the numerical and experimental results of Yamaguchi et al. (2000a, b) and Watanabe et al. (2002a, b).

Fig. 7 shows the results of a numerical simulation for $\bar{L} = 1000$ exactly at the critical speed ($\bar{U}_c = 1.542 \times 10^{-3}$) found in Fig. 6(d). The plate's motion can be compared with the corresponding results of the standard case in Fig. 4. The presence of the higher-order modes predicted by the state-space calculation is confirmed. This type of

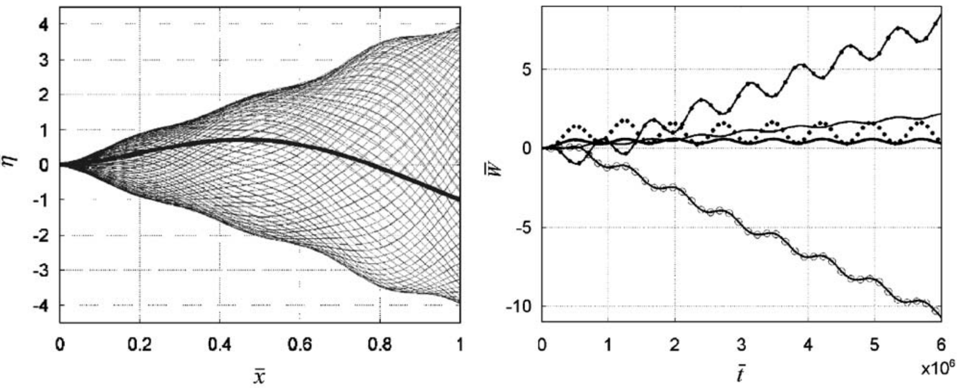

(a) (b)

Fig. 7. Fluid–structure behaviour at $\bar{L} = 1000$, $\bar{H} = 1$ (effectively isolated): numerical simulations of system behaviour with $\bar{d} = 0$ at the critical flow speed $\bar{U} = U_c = 1.542 \times 10^{-3}$, (a) time-sequence of instantaneous plate deformation (the thick line is the initially imposed deformation), and (b) time-variation of work done by fluid on plate, $\bar{W}$, in which —— (thin), –o–, –●– and ···, respectively, indicate the work done over the first, second, third and fourth quarters of the plate from its leading edge while —— (thick) is the sum of these contributions.

modal-coalescence flutter was illustrated as a travelling-wave form of flutter in Tang and Païdoussis (2007). The pressure loading is now more like that of potential flow over an infinitely long flexible plate. The magnitude of the pressure due to plate curvature plays the essential role in destabilisation by bringing the two modes to coalescence and thereby create the phase shift between pressure and plate motion that drives energy into the plate. Thus, instability of the plate now occurs when the flow speed is high enough to produce pressure forces of a sufficient magnitude to modify strongly the modal behaviour. As a travelling-wave instability, it should be most pronounced over the downstream regions of the plate because these locations are furthest from the leading-edge restraint that inhibits wave travel. The variation with time of work done by the fluid pressure is shown in Fig. 7(b). The result for the entire flexible plate confirms the state of neutral stability; there is no net transfer of energy between fluid and structure. However, it is also evident that there is energy transmission from fluid to structure over the downstream half and, to a much lesser extent, the first quarter of the flexible plate while the reverse occurs in the second quarter. Thus, the instability that sets in when $\bar{U}_c$ is exceeded can be described as (largely) *downstream-driven*, in contrast to the instability characteristics of a short plate ($\bar{L} = 1$) described earlier.

A series of numerical experiments to determine the critical flow speeds and associated critical modes within the range of mass ratios $0.2 \leqslant \bar{L} \leqslant 1000$ has been conducted to compare our results with those of other published work. Watanabe et al. (2002b) collected $\bar{U}_c$ data from several theoretical and experimental studies to compare against their own findings. These data have been re-plotted along with our results and are displayed in Fig. 8. The purpose of presenting this figure is twofold. It gives credence to the validity of our model and it summarises the overall trend of $\bar{U}_c$-dependence upon $\bar{L}$ for the fluid–structure system. Accordingly, we show only general trends and have not included all of the experimental and theoretical data published. For a complete collection of results published to date, the excellent summary figure in Tang and Païdoussis (2007) is recommended. Our values of $\bar{U}_c$ in Fig. 8 show good correlation with the other theoretical models. When comparing theory and experiment, it is noted that all models capture the overall trend of the experimental data. As $\bar{L}$ increases the fluid–structure system becomes unstable at successively lower values of nondimensional flow speed. All models correctly predict that instabilities above $\bar{U}_c$ are of the flutter type as observed in experiments; we additionally note the point of transition from single-mode flutter to the modal-coalescence type at the bottom of the figure. However, all models fail to capture hysteresis effects found in experiments where several values of $\bar{U}_c$ can be obtained for a single value of $\bar{L}$. This is most probably due to the existence of a sub-critical instability in the system that cannot be captured by linear models. The large disparity between experimental measurements of $\bar{U}_c$ and those theoretically predicted may be due to the omission of three-dimensional effects. The analysis of Eloy et al. (2007) modelled transverse plane waves on a plate of finite aspect ratio showing that two-dimensional analyses, at infinite aspect ratio, grossly overestimate the pressure loading and thus give unrealistically low critical flow speeds for instability onset. When the finite aspect ratio is taken into account, their Fig. 6 shows that theory and experiment are well-aligned for aspect ratios less than unity. For higher aspect ratios, agreement was less good but, as Eloy et al. noted, this may be due to the existence of three-dimensional deflections of the plate in a physical system. For the related problem of a three-dimensional flexible plate held along each of its edges in one-sided flow, these effects were also reported by Lucey and Carpenter (1993b). Additionally, nearly all of the theoretical models do not model viscous effects explicitly. For large-amplitude motions, time-varying separation (upstream of the trailing edge) of the boundary-layer may occur that could create a further type of flutter mechanism.

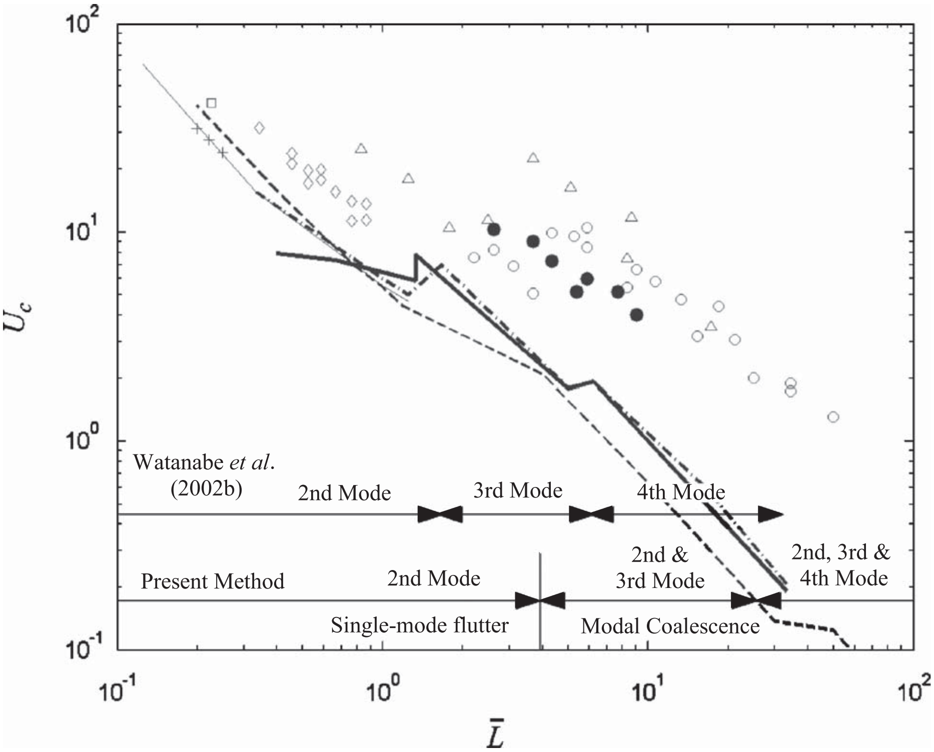

Fig. 8. Fluid–structure behaviour for a range of $\bar{L}$ at $\bar{H} = 1$ (effectively isolated): plot of U_c at different $\bar{L}$ (adapted from Watanabe et al. (2002b)). Data are from several published studies. Experimental data: From Watanabe et al. (2002b): ○ flag type paper, ● long-type paper, △ elastic sheet; ◇ Huang (1995); + Kornecki et al. (1976); theoretical models: □ Kornecki et al. (1976); – (thin) Huang (1995); – (thick) Guo and Païdoussis (2000); –· Watanabe et al. (2002b) with their parameter $C_D = 0$; –– present theory. The first set of boundaries at the bottom of the graph show the predominant *in vacuo* eigenmode in the form of the critical mode calculated by the theoretical model of Watanabe et al. (2002b); the second set of boundaries are from our numerical simulations, also showing the predominant eigenmode when the flutter instability predicted is of the single-mode type, but also showing which group of modes form the critical mode when the flutter instability is of the modal-coalescence type.

Finally, we note from Fig. 8 that our predictions of the dominant eigenmodes in the form of the critical mode and those of Watanabe et al. (2002b) differ significantly at higher values of $\bar{L}$. This is because Watanabe et al. (2002b) presupposed that the motion of the plate could be made up of the amalgamation of the first four *in vacuo* eigenmodes. In our model there is no such pre-supposition. As $\bar{L}$ increases the critical mode becomes more complex and its correspondence to a single *in vacuo* plate mode becomes increasingly untenable. Our computations capture the fluid–structure eigenmodes directly; at high $\bar{L}$ these may be very different to those that can be constructed from a limited set of *in vacuo* plate modes. Additionally, Figs. 6(a)–(d) show that as $\bar{L}$ increases, clear changes (or 'modal switching') of the critical mode do not occur. While the single-mode flutter of short plates may be dominated by recognisable *in vacuo* eigenmodes (principally the second), the modal-coalescence flutter instability of long plates has been shown to comprise at least two *fluid-loaded* eigenmodes of flexible plate. For long plates the change of critical mode shape evolves in a continuous manner with $\bar{L}$.

3.2. Variation of unsteady model parameters at $\bar{L} = 1$

The fluid–structure dynamics of an effectively isolated ($\bar{H} = 1$) flexible plate have been elucidated in Section 3.1. We now investigate the effects of including additional features in the fluid–structure model for the case of $\bar{L} = 1$. Thus, we incorporate: (a) an unsteady wake, (b) channels walls, and (c) a rigid-inlet surface upstream of the flexible plate. Discussion of the results in this section focuses on how these additional features modify the critical speed and dynamics of the 'standard' $\bar{L} = 1$, $\bar{H} = 1$ case.

The effect of including an unsteady wake is illustrated by the results of Fig. 9. The validation of the linearised, discrete-vortex method and its coupling with a fixed-geometry BEM is presented in Howell (2006). The effect of the shed vorticity increases the critical speed, $\bar{U}_c$ (for the standard case $\bar{L}=1$, $\bar{H}=1$) from 5.452 to 5.948, an increase of approximately 9%. The shed vorticity increases the magnitude of the fluid pressure near the trailing edge due to the terms $\dot{u}^{Nb}$ and u^{Nb} in Eq. (19). The wider neck of the mode shape seen in Fig. 9(a), as compared with that of Fig. 4(a), indicates an increased component of lower-order modes; this is borne out by an oscillation frequency, $\bar{\bar{\omega}}$, of 0.61 as compared with 0.69 for the standard case. These changes are consistent with the increased pressure loading near the trailing edge of the plate when the wake effects are included.

At first sight, an increased magnitude of the fluid pressure near the trailing edge might seem incompatible with stabilisation as evidenced by the increase in critical speed. However, we recall that the single-mode flutter of this short plate arises not from the magnitude of the pressure force but from its phase relationship with the plate's motion. Because the wake is a periodic continuation of the bound vorticity, it exercises an effect that is similar to that of increased plate length on the phase relation between the pressure acting on the plate and its velocity. Thus, the pressure and velocity signals are closer to being orthogonal when the wake is included and this reduces the potency of the phase-shift mechanism of the single-mode flutter of short plates. However, its inclusion does not eliminate single-mode flutter (nor replace it with modal-coalescence flutter as would increasing plate length). The modification of the phase between pressure and plate velocity, effected by the wake, reduces the rate of energy transfer between fluid flow and structure and this leads to an increase in the critical speed for short plates. This is demonstrated by Fig. 9(b) in which we have plotted the energy transfers for each of the four quarters of the plate with and without the wake included. The flow is at the critical speed $\bar{U}=5.452$ that is obtained without a wake and thus the mean value of the total $\bar{W}$ for the wake results is marginally decreasing thereby indicating an attenuating response at this flow speed. As would be expected the greatest reductions in the energy-transfer mechanism are seen to occur in the third and fourth quarters of the flexible plate that are most strongly influenced by the wake vorticity. Table 1 lists the values of the critical speed with, $\bar{U}_c^*$, and without,

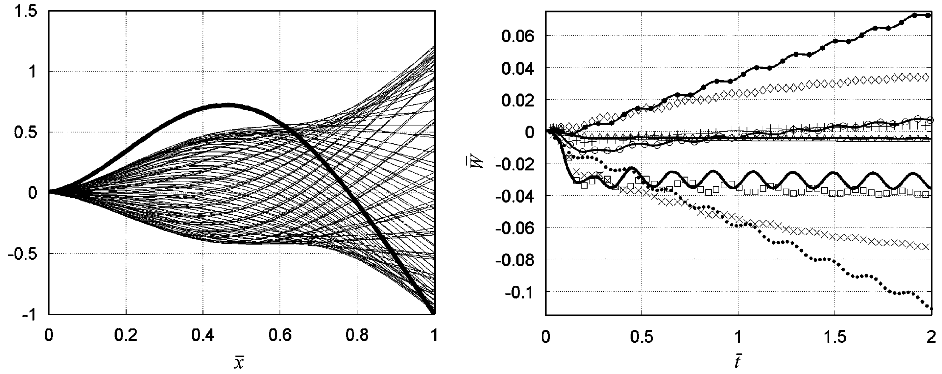

(a) (b)

Fig. 9. The effect of an unsteady wake on the system response: numerical simulations of system behaviour at $\bar{L}=1$, $\bar{H}=1$ (effectively isolated) and $\bar{d}=0$, (a) time-sequence of instantaneous plate deformation at the new critical flow speed $\bar{U}_c=5.948$ (the thick line is the initially imposed deformation and note that early deformations have been removed to provide a clearer view of the critical mode), and (b) time-variation of work done by fluid on plate, $\bar{W}$, with (discrete data) and without (continuous data) a wake at $\bar{U}_c=5.452$ (the critical speed found without a wake) where the data sequences △, +, ◇, × and —— (thin), -o-, -●-, ··· each, respectively, indicate the work done over the first, second, third and fourth quarters of the plate from its leading edge, while □ and —— (thick) are the respective sums of these contributions.

Table 1
Effect of an unsteady wake on the critical velocity: variation of the critical velocity, $\bar{U}_c$, with $\bar{L}$; $\bar{U}_c^*$ is the critical velocity when the unsteady wake effect is included.

$\bar{L}$	$\bar{U}_c$	$\bar{U}_c^*$	$(\bar{U}_c^*-\bar{U}_c)/\bar{U}_c$
0.2	40.2000	54.3800	0.35
0.6	9.6400	11.4700	0.19
1.0	5.4520	5.9480	0.09
1.2	4.5846	4.7269	0.03
1.4	4.0123	3.9533	−0.01
1.6	3.6312	3.4385	−0.05

$\bar{U}_c$, the wake effects, along with the proportional difference $(\bar{U}_c^* - \bar{U}_c)/\bar{U}_c$, for a range of $\bar{L}$. These data corroborate the discussion above by demonstrating that wake effects are stabilising for short plates. Longer plates are less affected by the wake but experience a destabilising effect because they succumb to modal-coalescence flutter that results from the pressure and plate velocity signals being more closely orthogonal.

The effect of a rigid central surface, equal in length to the flexible surface, placed upstream of the flexible surface and in the effective absence of channel walls ($\bar{H} = 1$) is now investigated. Figure 10 maps the variation of system eigenmodes with flow speed for the present case and can be contrasted with Fig. 3(a); similarly, Figs. 11(a) and (b) show the critical mode and energy transfer from fluid to structure, respectively, and can be compared with the corresponding results of the standard case in Figs. 4(a) and (c). We note that the third mode (marked 3) of the fluid–structure system is the first to become unstable, $\bar{\omega}_R > 0$ for $\bar{U} > \bar{U}_c = 13.547$. The critical speed is substantially higher than $\bar{U}_c = 5.452$ found in the absence of a rigid central surface. The inclusion of the rigid central surface stabilises the second-mode flutter that was previously critical. That single-mode flutter was shown to be caused by the phase relationship between fluid pressure and plate velocity that can be attributed in part to the effect of high flow curvature caused by the leading-

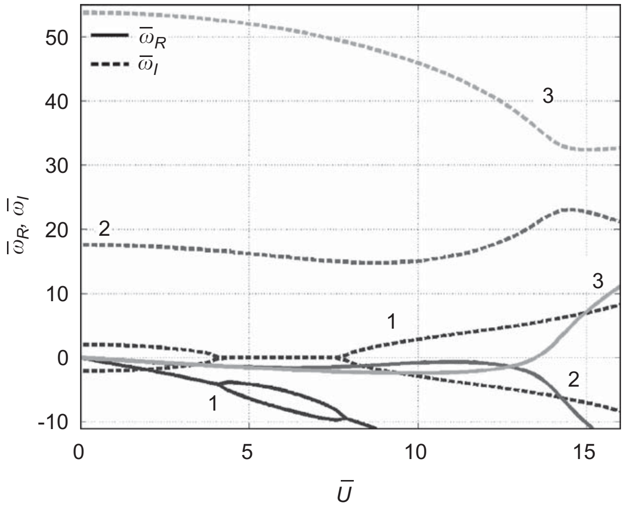

Fig. 10. The effect of an upstream, rigid central-surface on the system response: variation of system eigenmodes with flow speed for $\bar{L} = 1$, $\bar{H} = 1$ (effectively isolated) and $\bar{d} = 0$ when an upstream, rigid central-surface (equal in length to the flexible plate) is introduced. The numbers on each figure identify the mode number in order of ascending frequency at $\bar{U} = 0$.

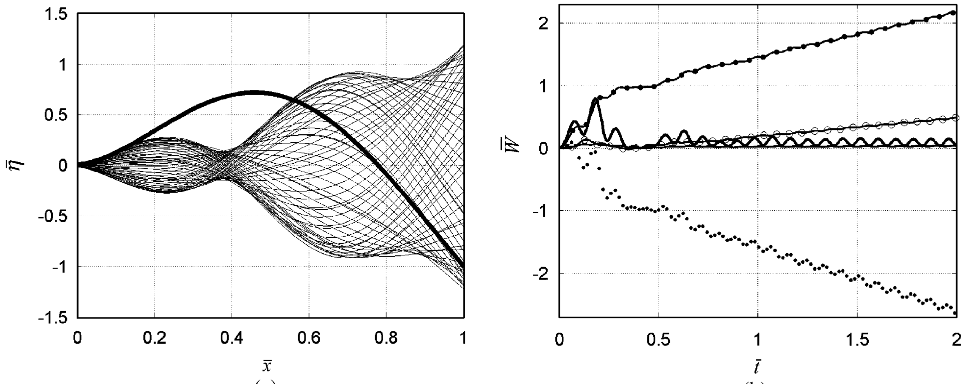

(a) (b)

Fig. 11. The effect of an upstream, rigid central-surface on the system response: numerical simulation of system behaviour for $\bar{L} = 1$, $\bar{H} = 1$ (effectively isolated) and $\bar{d} = 0$ at the new critical flow speed $\bar{U}_c = 13.547$, (a) time-sequence of instantaneous plate deformation (the thick line is the initially imposed deformation), and (b) time-variation of work done by fluid on plate, $\bar{W}$, in which —— (thin), —○—, —●— and · · ·, respectively, indicate the work done over the first, second, third and fourth quarters of the plate from its leading edge while —— (thick) is the sum of these contributions.

edge singularity. The introduction of a rigid central-surface moves the singularity much further upstream of the flexible plate and that destabilisation mechanism is diminished. The principal instability mechanism is now seen in Fig. 10 to be a modal-coalescence of Modes 2 and 3 and this is clearly reflected in the mode shape of Fig. 11(a). Thus, the flexible plate behaves in a way that is closer to that of a plate with high $\bar{L}$ — see Figs. 6 and 7. This then suggests that the effect of an upstream rigid plate of fixed length decreases as $\bar{L}$ is increased, a result that was shown by Tang and Païdoussis (2007). What is perhaps surprising in the present results is that the greatest destabilising energy transfer continues to occur in the middle half of the plate as shown in Fig. 11(b), even though the instability is now essentially a modal-coalescence flutter.

The effect of channel walls is now investigated. These are placed at a distance of one-tenth of the plate length from the plate and thus $\bar{H} = 0.1$. Plots of the critical mode and the energy-transfer from fluid to wall are presented in Fig. 12. The proximity of the walls when $\bar{L} = 1$ reduces $\bar{U}_c$ by 5% relative to the isolated case. This configuration in which channel-wall proximity affects the behaviour and stability of the flexible plate has been studied by Aurégan and Depollier (1995) and Guo and Païdoussis (2000). The lowering of $\bar{U}_c$, relative to the isolated case, is caused by an increase in the pressure difference across the plate that occurs through mass-conservation and Bernoulli effects in a channel of finite width. This supplements the pressure difference caused by plate curvature and motion, the only sources of pressure difference when channel walls are absent. However, the channel walls do not significantly modify the location of the greatest amount of fluid work done on the plate; see Fig. 12(b). Like the standard case of Section 3.1, energy transfer from fluid to structure occurs in the second and third quarters of the plate while the reverse occurs in the downstream quarter. Accordingly we can continue to describe the destabilisation as being *mid-plate-driven*. The effect of the channel walls is also seen in the form of the critical mode plotted in Fig. 12(a) that has both a wider neck and higher amplitude (relative to the same form of initial excitation) as compared to its counterpart in Fig. 4(a).

3.3. Potential snores

The computational model is now used to study a particular application of the foregoing fluid–structure interactions. In doing so, however, we are able to illustrate the general effects of time-varying mean flow and inhomogeneity in the properties of the flexible plate. The geometry shown in Fig. 1 is assumed to be an approximation of the human pharynx: the channel walls represent the throat, a rigid-inlet the hard palate and the flexible plate is the soft palate. We are therefore able to model the basic features of human snoring where such snores are directly related to flutter of the soft palate. Similar approaches to modelling human snoring have been made by Gavriely and Jensen (1993), Aurégan and Depollier (1995), Huang (1995), Balint and Lucey (2005) and Tetlow and Lucey (2009). Appropriate nondimensional parameters based on human dimensions are $\bar{L} = 0.42$ and $\bar{H} = 0.1$. It is assumed a snore is initiated when the oscillation of the plate becomes unstable, i.e. above $\bar{U}_c$.

We first study the effect of using a time-varying mean flow $\bar{U}(\bar{t})$ that approximately models inhalation during sleep. The inhalation lasts for 1 s (or 4.28 units of nondimensional time), during which time $\bar{U}$ increases linearly from zero to a

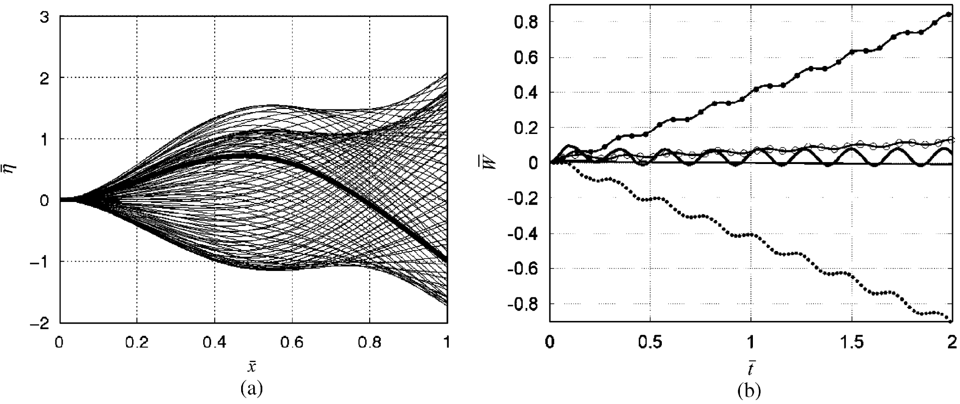

(a) (b)

Fig. 12. The effect of channel walls on the system response: numerical simulation of system behaviour for $\bar{L} = 1$, $\bar{H} = 0.1$ and $\bar{d} = 0$ at the new critical flow speed $\bar{U}_c = 5.177$, (a) time-sequence of instantaneous plate deformation (the thick line is the initially imposed deformation), and (b) time-variation of work done by fluid on plate, $\bar{W}$, in which —— (thin), -○-, -●- and ···, respectively, indicate the work done over the first, second, third and fourth quarters of the plate from its leading edge while —— (thick) is the sum of these contributions.

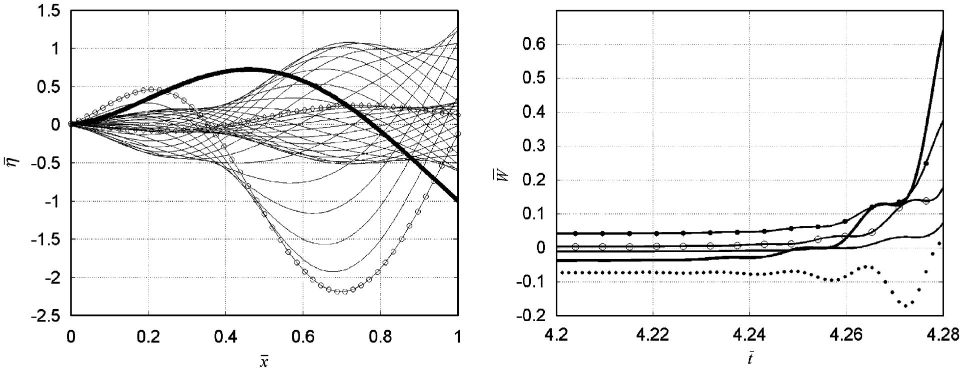

(a) (b)

Fig. 13. The effect of time-varying uniform flow on the system response: numerical simulation of system behaviour for $\bar{L} = 0.42$, $\bar{H} = 0.1$ (these dimensions mimicking that of the human upper airway) and $\bar{d} = 0$ with an upstream rigid central surface (equal in length to the flexible plate) present, (a) time-sequence of instantaneous plate deformation (the thick line is the initially imposed deformation while —◇— and —○— denote deformations at $\bar{t} = 4.24$ and 4.28, respectively, and deformations prior to this time period have been removed to provide a clearer view of the critical mode that develops), and (b) time-variation of work done by fluid on plate, $\bar{W}$, in which —— (thin), —○—, —●— and ···, respectively, indicate the work done over the first, second, third and fourth quarters of the plate from its leading edge while —— (thick) is the sum of these contributions. $\bar{U}(\bar{t})$ increases from 0 to 41.8 over the period $\bar{t}: 0 \rightarrow 4.28$.

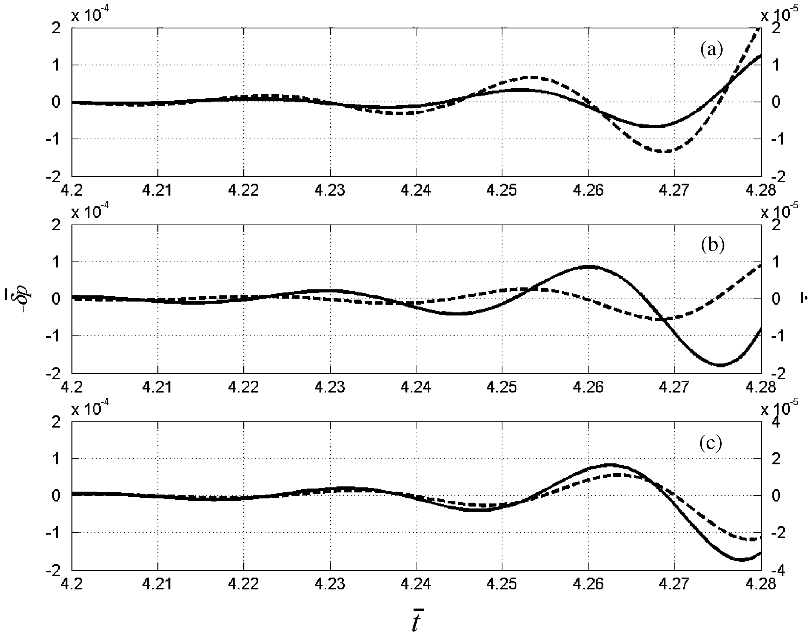

Fig. 14. The effect of time-varying uniform flow on the system response: variation of perturbation pressure, $-\bar{\delta p}$ (dashed line), and plate velocity, $\dot{\bar{\eta}}$ (continuous line) with time at (a) $\bar{x} = 0.3$, (b) $\bar{x} = 0.5$, and $\bar{x} = 0.7$ for the numerical simulation that yielded Fig. 13.

chosen maximum velocity. Therefore, a *critical velocity gradient* exists; this is the maximum velocity gradient for which the flexible surface is still stable at the end of the 'inhalation'. The development of the critical mode is illustrated in Fig. 13(a) that shows a series of instantaneous deflections of the flexible plate between the times $\bar{t} = 4.24$ and 4.28. The run commenced at $\bar{t} = 0$ with the plate's second *in vacuo* mode applied as an initial deflection; this is also plotted in Fig. 13(a). The applied initial deflection decays but from it emerges a higher-order system mode of the type promoted by increased fluid loading in Section 3.1 and the inclusion of an upstream rigid surface in Section 3.2. This is evident first in the appearance of the envelope of deflections seen in Fig. 13(a) that is formed at times for which $\bar{U}(\bar{t})$ is close to those which yield neutral stability. However, because the flow speed continues to increase to its maximum applied value at $\bar{U}(4.28)$, strong amplification is then seen in the series of final instantaneous deflections. The emergence of a higher-order mode as that which destabilises the system suggests a modal-coalescence flutter mechanism that we have shown earlier to be promoted by increasing fluid loading or plate length for a steady applied flow. In the present case the increased fluid loading arises from a much higher final flow speed, $\bar{U} = 41.8$, at $\bar{t} = 4.28$ (3.7 m/s after 1 s), than would have been required to destabilise the second mode had a steady flow speed of $\bar{U} = 26.5$ (2.34 m/s) been applied. Figure 13(b) shows the associated time-variation of fluid work done $\bar{W}$ over the period that culminates in the end of inhalation for the critical velocity gradient. It is clear that the instability is driven by the fluid work done on the third, second and first quarters of the plate in order of the magnitude of contribution to the plate's destabilisation. Figure 14 shows the time-variation of flexible-surface velocity and fluid pressure over the same time period as plotted in Fig. 13. At the location $\bar{x} = 0.7$ in Fig. 14(c) that resides within the third quarter where the greatest destabilising work occurs, it is seen that $(-\delta\bar{p})$ and $\dot{\bar{\eta}}$ are almost in-phase. This provides further evidence for characterising the instability as being of the modal-coalescence type since exact phase alignment indicates a pure resonance of fluid loading and plate motion. Finally, we recognise that the critical velocity gradient found is specific to the initial excitation applied. As evident from Fig. 13(a), we applied the second *in vacuo* mode that might have been expected to promote flutter of the second system mode. What we therefore emphasise is that the single-mode flutter mechanism that has been seen to be the critical instability for short plates in steady uniform flow may not establish itself in a time-varying mean flow. Thus, the critical instability is likely to be the more robust modal-coalescence instability that typically occurs at higher mean-flow dynamic pressures.

We now briefly investigate the effect of spatially varying plate stiffness for the case of uniform mean flow. The critical speed for a homogeneous flexible plate in a system with $\bar{L} = 0.42$ and $\bar{H} = 0.1$ is first found. The evaluation of $\bar{W}$, see Fig. 15(a), indicates that the instability causing this snore is driven solely by energy transfer on the third quarter of the

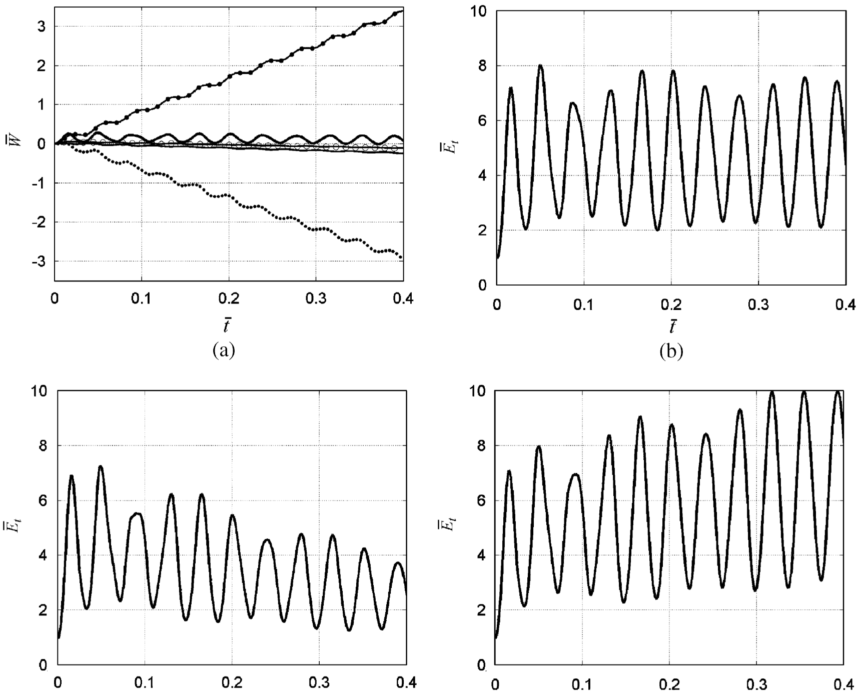

(a) (b)

(c) (d)

Fig. 15. The effect of spatially varying plate stiffness on the system response: numerical simulation of system behaviour for $\bar{L} = 0.42$, $\bar{H} = 0.1$ (these dimensions mimicking that of the human upper airway) and $\bar{d} = 0$ with an upstream rigid central surface (equal in length to the flexible plate) present, (a) homogeneous flexible plate at its critical flow speed $\bar{U}_c = 26.5$: time-variation of work done by fluid on plate, $\bar{W}$, in which —— (thin), —○—, —●— and ···, respectively, indicate the work done over the first, second, third and fourth quarters of the plate from its leading edge while —— (thick) is the sum of these contributions, and variation of plate energy with time at $\bar{U} = 26.5$ for (b) homogeneous flexible plate, (c) flexible plate with a 10% increase in plate stiffness over its third quarter, and (d) flexible plate with a 10% increase in plate stiffness over its first quarter.

plate, the characteristic similar to that seen in Fig. 12(b) ($\bar{L} = 1$, $\bar{H} = 0.1$) but with no assistance from the second quarter of the plate. The plate energy, $\bar{E}_t$, for this case is shown in Fig. 15(b) and is seen to maintain a constant mean value appropriate to the neutrally stable state of the plate. We then mimic a proposed 'cure' for the snore by applying a 10% greater stiffness in the third quarter of the flexible surface where the instability mechanism occurs. This soft-palate stiffening is a strategy similar to that described by Ellis et al. (1993). The resulting trace of plate energy is shown in Fig. 15(c) and the strategy is indeed found to have a stabilising effect. If the same simulated stiffening is applied to the first quarter of the flexible plate instead of the third quarter, the result of Fig. 15(d) shows that the change is actually destabilising. These results demonstrate that flexible-plate stiffening can be used to control stability for the alleviation of palatal snoring but that the location of such stiffening is critical in order to achieve the desired effects.

4. Conclusions

We have developed and deployed a new computational model for the fluid–structure interaction between a cantilevered-free flexible plate and an ideal flow. The model permits numerical simulations to be conducted that capture transient behaviour and in which spatially localised fluid–structure interactions can be identified. The computational model can also be used to determine the global stability of the system for the infinite-time limit. Using these solution methods in combination we have elucidated instability mechanisms showing how spatially varying fluid–structure interactions along the plate combine to give the system response.

The investigations presented in this paper provide an accurate linear-stability map for the standard case of cantilevered-free flexible plate in an unbounded uniform flow. We have then investigated the changes to this 'standard' fluid–structure interaction that are caused by the effects of: (a) shed vorticity, (b) channel walls, (c) a rigid-inlet surface, (d) temporally varying inlet flow-velocity, and (e) variable plate stiffness. A summary of the effects of (a)–(c) is given in Table 2. Overall, we can conclude that short flexible plates are destabilised by single-mode flutter caused by an irreversible energy transfer from fluid to structure that principally occurs over the middle part of the flexible plate. In contrast, long flexible plates succumb to a modal-coalescence flutter that is principally driven by the magnitude of the fluid loading as opposed to the subtle phase relationships that underpin single-mode flutter. Thus, the modal-coalescence flutter has its parallel in the Kelvin–Helmholtz instability of flexible plates held at both ends at flow speeds higher than those that give divergence instability. The proximity of channel walls tends to intensify the single-mode flutter mechanism whereas the inclusion of a rigid-inlet surface diminishes the mechanism so that a higher critical flow speed associated with modal-coalescence is reached before instability sets in. The effect of a wake is to decrease the potency of the single-mode flutter mechanism that dominates the destabilisation of short plates with light fluid loading and thereby increase critical speeds. However, wake effects promote the modal-coalescence flutter that is the critical instability for long plates or those with heavy fluid loading and are therefore destabilising; the magnitude of this effect reduces with increases to plate length.

By elucidating the instability mechanisms to which the fluid–structure system is prone, we have identified two distinct types of plate flutter. While the energy flow between fluid and structure for both is caused by phase-shifts between the pressure load and the motion of the plate, the mechanics behind the phase shifts are very different. This has implications for the engineering control (or exploitation) of the instabilities. Structural forces are dominant in the single-mode flutter

Table 2
Summary of flutter instability dependence upon system configuration.

Simulation description	$\bar{L}$	$\bar{H}$	% change in U_c from 'standard' case	$\bar{\bar{\omega}}$	Region of plate where most destabilising energy transfer occurs	(Incipient) Flutter type
Standard	1	$1(=\infty)$	–	0.69	Middle half	Single-mode
Long plate/heavy fluid loading	1000	$1(=\infty)$	−99.97%	0.19	Mainly downstream half	Modal-coalescence
Wake included	1	$1(=\infty)$	9.10%	0.61	Middle half	Single-mode
Rigid, upstream central-surface	1	$1(=\infty)$	148.48%	1.64	Middle half	Modal-coalescence
Channel flow	1	0.1	−5.04%	0.63	Middle half	Single-mode

of short plates and it is the phase-relationship (to plate motion), as opposed to the magnitude, of the fluid pressure that is critical. Thus, this instability, as we have shown, can be controlled by the judicious stiffening of parts of the plate or the inclusion of damping, for example, by doping the plate material. In contrast, the appearance of the destabilising phase shift in modal-coalescence flutter is principally dependent upon the magnitude of the pressure load that brings the coalescing modes together. Thus, damping has only a mildly modifying effect on the critical speed. Localised stiffening strategies, as a means to design out the instability, would also be difficult to implement. The added stiffness would need to be applied in such a way that it separated out the principal modes in the frequency space in order to postpone their coalescence with increasing flow speed.

The effects of time-varying mean flow and of spatially varying flexible-plate properties have been illustrated in the context of upper-airway dynamics and the mechanisms that might lie behind palatal snoring. We have shown that stiffening does have the potential to increase the critical speed of palatal flutter provided that it is applied in the correct location. This highlights the difficulty of applying successful treatment to a patient suffering from palatal snoring. This difficulty is compounded by the potential existence of two different types of instability that we have highlighted in this paper. Increasing complexity occurs when a more faithful representation of the upper airway is modelled. Aurégan and Depollier (1995) introduced two broad classifications namely, *pure* and *apnœic* snores, owing to the flexibility of the soft palate and channel properties, respectively. Moreover, the site of snore generation is not necessarily confined to the region of the soft palate but to various sites in the human pharynx, as shown by Miyazaki et al. (1998). It therefore follows that there will be different treatments for each type of snore and that treatment must be tailored to the individual patient. Fundamental understanding of the fluid–structure interactions at work undoubtedly will underpin the appropriate developments of such treatments.

Acknowledgements

Much of the work described in this paper was carried out while R.M.H. was in receipt of an EPSRC grant at the University of Warwick and during periods as a visiting academic hosted by Curtin University of Technology. The remaining authors dedicate this paper to the memory of Professor Peter Carpenter who passed away in April 2008.

References

Argentina, M., Mahadevan, L., 2005. Fluid-flow-induced flutter of a flag. Proceedings of the National Academy of Sciences of the United States of America 102 (6), 1829–1834.

Aurégan, Y., Depollier, C., 1995. Snoring: linear stability analysis and in vitro experiments. Journal of Sound and Vibration 188 (1), 39–54.

Balint, T.S., Lucey, A.D., 2005. Instability of a cantilevered flexible plate in viscous channel flow. Journal of Fluids and Structures 20 (7), 893–912.

Carpenter, P.W., Garrad, A.D., 1985. The hydrodynamic stability of flow over Kramer-type compliant surfaces. Part 1. Tollmien–Schlichting instabilities. Journal of Fluid Mechanics 155, 465–510.

Chorin, A.J., 1973. Numerical study of slightly viscous flow. Journal of Fluid Mechanics 57 (4), 785–796.

Crighton, D.G., Oswell, J.E., 1991. Fluid loading with mean flow. I. Response of an elastic plate to localized excitation. Philosophical Transactions of the Royal Society of London A 335, 557–592.

Doaré, O., de Langre, E., 2002. Local and global instability of fluid-conveying pipes on elastic foundations. Journal of Fluids and Structures 16 (1), 1–14.

Doaré, O., de Langre, E., 2006. The role of boundary conditions in the instability of one-dimensional systems. European Journal Mechanics B/Fluids 25, 948–959.

Ellis, P.D.M., Ffowcs Williams, J.E., Shneerson, J.M., 1993. Surgical relief of snoring due to palatal flutter: a preliminary report. Annals of the Royal College of Surgeons of England 75, 286–290.

Eloy, C., Souilliez, C., Schouveiler, L., 2007. Flutter of a rectangular cantilevered plate. Journal of Fluids and Structures 23 (6), 904–919.

Gavriely, N., Jensen, O., 1993. Theory and measurement of snores. Journal of Applied Physiology 74 (6), 2828–2837.

Guo, C.Q., Païdoussis, M.P., 2000. Stability of rectangular plates with free side-edges in two-dimensional inviscid channel flow. Journal of Applied Mechanics 67, 171–176.

Howell, R.M., Lucey, A.D., Carpenter, P.W., 2004. Numerical simulation of a cantilevered flexible plate embedded in an unbounded inviscid flow. In: Axisa, F., de Langre, E. (Eds.), Proceedings of the 8th International Conference on Flow-Induced Vibrations, Paris, France, pp. 167–171.

Howell, R.M., 2006. Snoring: a flow–structure interaction. Ph.D. Thesis, University of Warwick.

Huang, L., 1995. Flutter of cantilevered plates in axial flow. Journal of Fluids and Structures 9, 127–147.

Kornecki, A., Dowell, E.H., O'Brien, J., 1976. On the aeroelastic instability of two-dimensional panels in uniform incompressible flow. Journal of Sound and Vibration 47 (2), 163–178.

Lucey, A.D., Carpenter, P.W., 1992. A numerical simulation of the interaction of a compliant wall and inviscid flow. Journal of Fluid Mechanics 234, 121–146.

Lucey, A.D., Carpenter, P.W., 1993a. On the difference between the hydroelastic instability of infinite and very long compliant panels. Journal of Sound and Vibration 163 (1), 176–181.

Lucey, A.D., Carpenter, P.W., 1993b. The hydroelastic stability of three-dimensional disturbances of a finite compliant panel. Journal of Sound and Vibration 165, 527–552.

Lucey, A.D., Cafolla, G.J., Carpenter, P.W., 1998. The effect of a boundary layer on the hydroelastic stability of a flexible wall. In: Horacek, J., Zolotarev, I. (Eds.), Proceedings of the 3rd International Conference on Engineering Hydroelasticity. Czech Technical University Press, pp. 268–273.

Miyazaki, S., Itasaka, Y., Ishikawa, K., Togawa, K., 1998. Acoustic analysis of snoring and the site of airway obstruction in sleep related respiratory disorders. Acta Oto-Laryngologica 118 (Suppl. 537), 47–51.

Pitman, M.W., Lucey, A.D., 2009. On the direct determination of the eigenmodes of finite flow-structure systems. Proceedings of the Royal Society A 465, 257–281.

Tang, L., Païdoussis, M.P., 2006. A numerical investigation on the dynamics of two-dimensional cantilevered flexible plates in axial flow. In: Proceedings of ASME Pressure Vessels and Piping Division Conference, Vancouver, BC, Canada, Paper no.: PVP2006-ICPVT11-93817.

Tang, L., Païdoussis, M.P., 2007. On the instability and the post-critical behaviour of two-dimensional cantilevered flexible plates in axial flow. Journal of Sound and Vibration 305, 97–115.

Tetlow, G.A., Lucey, A.D., 2009. Motions of a cantilevered flexible plate in viscous channel flow driven by a constant pressure drop. Communications in Numerical Methods in Engineering, doi:10.1002/cnm.1225.

Watanabe, Y., Suzuki, S., Sugihara, M., Sueoka, Y., 2002a. An experimental study of paper flutter. Journal of Fluids and Structures 16 (4), 529–542.

Watanabe, Y., Isogai, K., Suzuki, S., Sugihara, M., 2002b. A theoretical study of paper flutter. Journal of Fluids and Structures 16 (4), 543–560.

Weaver, D.S., Unny, T.E., 1970. The hydroelastic stability of a flat plate. ASME, Journal of Applied Mechanics 37 (1), 823–827.

Yamaguchi, N., Yokota, K., Tsujimoto, Y., 2000a. Flutter limits and behaviours of a flexible thin sheet in high speed flow — I: analytical method for prediction of the sheet behaviour. ASME Journal of Fluids Engineering 122, 65–73.

Yamaguchi, N., Sekiguchi, T., Yokota, K., Tsujimoto, Y., 2000b. Flutter limits and behaviours of a flexible thin sheet in high speed flow — II: experimental results and predicted behaviours for low mass ratios. ASME Journal of Fluids Engineering 122, 74–83.